Microbiology:

Structural and Biochemical Characterization of *Chlamydia trachomatis* Hypothetical Protein CT263 Supports that Menaquinone Synthesis Occurs through the Futalosine Pathway

Michael L. Barta, Keisha Thomas, Hongling Yuan, Scott Lovell, Kevin P. Battaile, Vern L. Schramm and P. Scott Hefty

J. Biol. Chem. published online September 24, 2014

JBC Papers in Press. Published on September 24, 2014 as Manuscript M114.594325
The latest version is at http://www.jbc.org/cgi/doi/10.1074/jbc.M114.594325

Structural and Biochemical Characterization of *Chlamydia trachomatis* Hypothetical Protein CT263 Supports that Menaquinone Synthesis Occurs through the Futalosine Pathway

Michael L. Barta[1], Keisha Thomas[2], Hongling Yuan[2], Scott Lovell[3], Kevin P. Battaile[4], Vern L. Schramm[2], P. Scott Hefty[1]

[1] Department of Molecular Biosciences, University of Kansas

[2] Department of Biochemistry, Albert Einstein College of Medicine of Yeshiva University

[3] Protein Structure Laboratory, Del Shankel Structural Biology Center, University of Kansas

[4] IMCA-CAT, Hauptman-Woodward Medical Research Institute

*Running Title**:*** *Crystal Structure of CT263 (MTAN) from C. trachomatis*

To whom correspondence should be addressed: P. Scott Hefty, Ph.D., 1200 Sunnyside Avenue, University of Kansas, Lawrence, KS 66045; Phone: 785-864-5392; Fax: 785-864-5294; Email: pshefty@ku.edu

Keywords: *Chlamydia*, quinones, crystallography, enzyme kinetics, nucleosidase, futalosine pathway

Background: Specific pathways and components for respiration in *Chlamydia* are poorly understood.
Results: *C. trachomatis* hypothetical protein CT263 crystal structure displays strong structural similarity with 5′-methylthioadenosine nucleosidase enzymes.
Conclusion: Bioinformatic analyses and enzymatic characterization of CT263 suggest menaquinone biosynthesis proceeds through the futalosine pathway in *Chlamydiaceae*.
Significance: Unique structural aspects of the CT263 active site can be leveraged to modify existing transition state inhibitors.

ABSTRACT

The obligate intracellular human pathogen *Chlamydia trachomatis* is the etiological agent of blinding trachoma and sexually transmitted disease. Genomic sequencing of *Chlamydia* indicated this medically important bacterium was not exclusively dependent on the host cell for energy. In order for the electron transport chain to function, electron shuttling between membrane embedded complexes requires lipid-soluble quinones (e.g. menaquionone or ubiquinone). The sources or biosynthetic pathways required to obtain these electron carriers within *C. trachomatis* are poorly understood. The 1.6 Å crystal structure of *C. trachomatis* hypothetical protein CT263 presented here supports a role in quinone biosynthesis. Although CT263 lacks sequence-based functional annotation, the crystal structure of CT263 displays striking structural similarity to 5′-methylthioadenosine nucleosidase (MTAN) enzymes. While CT263 lacks the active site-associated dimer interface found in prototypical MTANs, co-crystal structures with product (adenine) or substrate (5′-methylthioadenosine) indicate that canonical active site residues are conserved. Enzymatic characterization of CT263 indicates that the futalosine pathway intermediate, 6-amino-6-deoxyfutalosine (k_{cat}/K_m = 1.8 x 10^3 M^{-1} s^{-1}) but not prototypical MTAN substrates (e.g. *S*-adenosylhomocysteine and 5′-methylthioadenosine), are hydrolyzed. Bioinformatic analyses of the chlamydial proteome also support the futalosine pathway towards the synthesis of menaquinone in *Chlamydiaceae*. This report provides the first experimental support for quinone synthesis in

***Chlamydia*. Menaquinone synthesis provides another target for agents to combat *C. trachomatis* infection.**

Quinones are lipid-soluble electron carriers essential to cellular respiration in bacteria (1). While certain bacteria (e.g. *E. coli*) utilize different quinones depending on oxygen availability, many Gram-negative and most Gram-positive bacteria rely on menaquionone (MK) as the sole electron carrier (2). In higher order eukaryota MK (also known as Vitamin K_2) is a cofactor required for post-translational glutamate modification essential to a variety of regulatory pathways, including blood coagulation and bone metabolism (3). As humans are incapable of synthesizing MK, bacterial enzymes involved in this pathway are potential targets for the development of novel antimicrobial therapeutics.

Two distinct biosynthetic routes of MK have been described in bacteria (**Fig. 1**), the well-studied traditional route (4,5) and the recently discovered futalosine route (6). Both routes begin with chorismate, and involve common enzymes at several of the later steps. Importantly, no organism has been found to possess a complete set of enzymes required for both the traditional and futalosine MK biosynthetic routes (6). Thus, the presence of genes unique to either pathway indicates that complete routes are encoded. Human commensal bacteria, primarily facultative anaerobes (e.g. *Lactobacillus*) typically do not synthesize MK (7), and those that do (e.g. *E. coli*) utilize the traditional route. The absence of futalosine genes in these organisms strengthens the development of antimicrobial compounds targeting pathogenic bacteria which synthesize MK (8).

Chlamydia are obligate intracellular bacteria and include pathogenic species for which the requisite electron transport quinone is undetermined. The metabolically active form of *Chlamydia* replicates within a microaerophilic environment inside a modified intracellular vacuole (9). Early speculation suggested that *Chlamydia* acquire ubiquinone (UQ) from the host (10). However, genome sequencing indicated otherwise, revealing the presence of four UQ biosynthesis homologs that could play a role in quinone synthesis. As these predicted enzymes could potentially catalyze reactions found in both UQ and MK biosynthetic pathways, the predicted quinone biosynthetic pathway of *Chlamydia* has remained undefined. Previous reports suggested that *Chlamydia* possess futalosine enzyme homologs (8,11), but these genes were not specifically described. Here we present structural, enzymatic and bioinformatic evidence in support of *Chlamydiaceae* utilizing the futalosine route towards the synthesis of MK.

EXPERIMENTAL PROCEDURES

Cloning, Overexpression and Purification of Recombinant CT263 from Chlamydia trachomatis

A gene fragment encoding the entire open reading frame (residues 1–196) of CTL0515 was amplified from *C. trachomatis* (serovar L2 434/Bu) genomic DNA via PCR and subcloned into *BamH*I/*Not*I-digested pT7HmT (12). In keeping with consistent chlamydial nomenclature, all references to this gene product will utilize the *C. trachomatis* D/UW-3 homolog, CT263. CTL0515 and CT263 are 99% identical, with a single substitution (A76G) at the amino acid level. Upon DNA sequence confirmation, the vector was transformed into BL21(DE3) *E. coli* competent cells. This strain was grown to an OD_{600} of 0.8 at 37 °C within Terrific Broth supplemented with kanamycin (50 μg/ml), and protein expression was induced overnight at 16 °C by the addition of isopropyl 1-thio-β-D-galactopyranoside (IPTG) to a 1 mM final concentration. Bacterial cells were harvested by centrifugation, resuspended in lysis buffer (20 mM Tris-HCl (pH 8.0), 500 mM NaCl, and 10 mM imidazole), and then lysed by sonication. The soluble His_6-labeled protein was collected in the supernatant following centrifugation of the cell homogenate and purified on a Ni^{2+}-NTA-Sepharose column according to published protocols (12). Recombinant tobacco etch virus (TEV) protease was used to digest the fusion affinity tag from the target protein. Both the affinity tag and TEV protease were removed by reverse Ni^{2+}-NTA-Sepharose chromatography. After desalting into 20 mM Tris-HCl (pH 8.0), final purification was achieved by ResourceQ anion-exchange chromatography followed by size exclusion chromatography (GE Healthcare). The purified protein was concentrated to 10 mg/ml in 20 mM Tris-HCl (pH 8.0), 200 mM NaCl buffer by ultrafiltration and stored at 4 °C for further use.

Selenomethionine (SeMet)-substituted CT263 was grown according to standard protocols (13), purified as described above (all buffers contained 5 mM β-mercaptoethanol) and concentrated to 10 mg/ml in 20 mM Tris-HCl (pH 8.0), 200 mM NaCl buffer for crystallization.

Crystallization

Recombinant *C. trachomatis* CT263 was crystallized by vapor diffusion in Compact Jr. (Emerald Biosystems) sitting drop plates at 20 °C. Specifically, 0.5 µl of protein solution (10 mg/ml in 20 mM Tris-HCl (pH 8.0), 200 mM NaCl) was mixed with 0.5 µl of reservoir solution containing 200 mM ammonium sulfate, 100 mM sodium acetate trihydrate (pH 4.6) and 30% (w/v) PEG 2K MME, from the Crystal HT screen condition F1 (Hampton), and equilibrated against 75 µl of the latter. Single rectangular prism-shaped crystals appeared after 1 day and continued to grow for ~4 days. Crystals were flash-cooled in a cryoprotectant solution consisting of mother liquor with 20% (v/v) glycerol. Gold-derivatized CT263 crystals were generated by incubating native crystals for 24-48 hours in mother liquor supplemented with 10 mM K_2AuCl_4. Crystals that had changed to a yellow color (indicating the likely presence of ordered gold atoms) were harvested as described above.

SeMet-CT263 crystals were obtained in essentially the same manner as wild-type; however, small block-shaped crystals required reduced ammonium sulfate concentrations as well as increased pH and PEG 2K MME. Briefly, protein solution (0.5 µl) was mixed with 0.5 µl reservoir solution (50 mM ammonium sulfate, 100 mM BIS-TRIS (pH 6.4) and 32% (w/v) PEG 2K MME) and equilibrated against 100 µl of the later. Small block-shaped crystals were harvested as described above.

Ligand-bound CT263 crystals were obtained in a similar manner as wild-type. Briefly, CT263 (wild-type or D161N, 10 mg/ml) was incubated with 10 mM MTA on ice for 30 min prior to crystallization. The ligand/protein solution (0.5 µl) was then mixed with 0.5 µl of reservoir solution (200 mM ammonium sulfate, 100 mM sodium acetate trihydrate (pH 4.6) and 30% (w/v) PEG 2K MME) and equilibrated against 100 µl of the later. Large block-shaped crystals were harvested in a similar manner as described above.

Diffraction Data Collection, Structure Determination, Refinement and Analysis

X-ray diffraction data were collected on all CT263 crystals at 1.000 Å at 100K with the exception of CT263-Au and SeMet-CT263 crystals, which were collected at 1.03969 Å and 0.97911 Å respectively, using a Dectris Pilatus 6M pixel array detector at IMCA-CAT beamline 17ID at the APS (**Table II**). Following data collection, individual reflections from each dataset were integrated with XDS (14). Laue class analysis and data scaling were performed with Aimless (15), which suggested the Laue class was *mmm*. Systematic absences were analyzed and suggested that the likely space group was $P22_12_1$ for all datasets with the exception of SeMet-CT263 ($P2_122_1$). The axes were permuted to $P2_12_12$ using Reindex Reflections in CCP4 (16) for all datasets, except SeMet-CT263, in order to adopt standard space group nomenclature.

Experimental phase information was obtained for the CT263 structure by Au-SAD using AutoSol within the Phenix suite (17,18), which identified 2 unique Au atoms in the asymmetric unit. Phenix.Autobuild correctly traced 269/392 Cα atoms (Map-model CC = 0.70, R_{work}/R_{free} = 38.57/43.00) within two CT263 polypeptides. Anomalous phases were combined with the complete 1.58 Å diffraction dataset using CAD (16). Subsequently, Phenix.Autobuild (17,18) was then used to trace 309/392 of the expected amino acids from the combined experimental maps with R_{work}/R_{free} = 26.74/29.77.

The structure of SeMet-CT263 was independently determined by Se-SAD using AutoSol within the Phenix suite (17,18), which identified 8 unique Se atoms in the asymmetric unit. Phenix.Autobuild correctly traced 353/392 Cα atoms (Map-model CC = 0.85, R_{work}/R_{free} = 21.00/24.98) within two CT263 polypeptides.

Chains A and B of Protein Data Bank (PDB) entry 4QAQ (wild-type *C. trachomatis* CT263) were used as a search model for WT/ADE, apo-$CT263^{D161N}$ and $CT263^{D161N}$/MTA structures.

Structure refinement was carried out using Phenix (17,18) for all structures. One round of individual coordinates and isotropic atomic

displacement factor refinement was conducted, and the refined model was used to calculate both $2F_o$-F_c and F_o-F_c difference maps. These maps were used to iteratively improve the model by manual building with Coot (19,20) followed by subsequent refinement cycles. TLS refinement (21) was incorporated in the final stages to model anisotropic atomic displacement parameters. Ordered solvent molecules were added according to the default criteria of Phenix and inspected manually using Coot prior to model completion. Interpretable electron density was absent for the following residues in each structure: apo-WT, chain A, 196 and chain B, 96-101 and 195-196; apo-D161N, chain B, 97-101, 129-130 and 195-196; SeMet-CT263, chain A, 195-196 and chain B, 97-101, 124-126 and 195-196; WT/ADE, chain A, 196, chain B, 96-102 and 195-196; D161N/MTA, chain A, 196 and chain B, 97-100 and 195-196. Disordered side chains were truncated to the point where electron density could be observed. Additional information and refinement statistics are presented in **Table II**.

Enzymatic Assay of CT263

Enzymatic assays were performed in 50 mM HEPES (pH 7.4), 200 mM KCl, 5% (v/v) glycerol and initiated by the addition of recombinant CT263. CT263 was added to a 200 µl reaction volume at a final concentration of 250 nM. Enzymatic activity was tested against 50 µM of the following substrates: 6-amino-6-deoxyfutalosine (AFL), *S*-adenosylhomocysteine (SAH), 5′-methylthioadenosine (MTA) and adenosine triphosphate (ATP). Samples were incubated overnight at room temperature and assayed via HPLC. Product peaks were collected, dried on a speed vacuum and analyzed by mass spectroscopy.

Characterization of steady state kinetic parameters

Activity with AFL was continuously monitored by UV-Vis spectrophotometry at 263 nm. Reactions were performed in 1 ml volumes under similar reaction conditions as above with varying concentrations of AFL. Reactions were initiated by the addition of CT263 to final concentrations of 100 to 200 nM. A luciferase-coupled assay converted product adenine to ATP in 100 mM Tris-HCl (pH 7.7) (22). Briefly, luminescence (RUL) was converted to pMoles of adenine (correcting for background and fitted to a standard curve). Initial rate kinetics (substrate k_{cat} and K_m) were calculated by fitting to the Michaelis-Menten equation.

Multiple Sequence Alignments and Figure Modeling

Multiple sequence alignments were carried out using ClustalW (23) and aligned with secondary structure elements using ESPRIPT (24). Sequences identified by DALI analysis of the CT263 crystal structure and used in alignments, along with their respective GenBank™ accession numbers, were as follows: *Chlamydia trachomatis* serovar L2 434/Bu (166154474); *Chlamydia muridarum* Nigg (15835152); *Chlamydia felis* Fe-C/56 (89898433); *Chlamydia caviae* GPIC (29840145); *Chlamydia pneumoniae* CWL029 (4376692); *Chlamydia psittaci* 6BC (332287326); *Chlamydia pecorum* (566141550); *Helicobacter pylori* (15644719); *Arabidopsis thaliana* (332661576); *Francisella philomiragia* (167626574); *Sulfurimonas denitrificans* (78777589); *Staphylococcus aureus* (15924589); *Streptococcus pneumoniae* (15900866); *Vibrio cholera* (9656950); *Neisseria meningitidis* (15676665); *Salmonella enterica* (322713231) and *Escherichia coli* (1786354). Three-dimensional structures were superimposed using the Local-Global Alignment method (LGA) (25). The following MTAN structures were obtained from the PDB (26): *E. coli* (1Z5P), *V. cholera* (3DP9), *N. meningitidis* (3EEI), *S. pneumoniae* (3MMS), *H. pylori* (4BMZ), *S. enterica* (4F1W), *S. aureus* (4GMH), *F. philomiragia* (4JOS) and *S. denitrificans* (4JWT). Representations of all structures were generated using PyMol (27). Calculations of electrostatic potentials at the molecular surface were carried out using DELPHI (28). The program CONSURF was used to plot levels of amino acid sequence conservation on the molecular surface (29).

RESULTS

Bioinformatic Support of Futalosine Pathway in Chlamydiaceae

The medically important, human pathogen *Chlamydia trachomatis* is capable of oxidative-level phosphorylation, generating ATP through the

electron transport chain (30). However, the source of electron shuttling quinones has been unclear, and is further compounded by the presence of four genes with homology to enzymes common to both the ubiquinone (UQ) and menaquinone (MK) biosynthetic pathways (10). Recently, an alternative pathway towards the synthesis of MK (**Fig. 1**), named the futalosine pathway after the first metabolic intermediate, was described (6). This pathway was found in bacteria, including *Streptomyces*, *Helicobacter* and *Campylobacter* among others, that had previously incomplete UQ or MK biosynthetic routes.

Iterative BLAST searches of *Streptomyces* genes involved in the futalosine pathway against available *Chlamydia* genome sequences yielded statistically significant hits for 7 of the 8 enzymes (**Table I**), with only the nucleosidase step (fulfilled by MqnB or 5′-methylthioadenosine nucleosidase, MTAN) lacking an identified homolog. As previously reported (31), despite utilizing *S*-adenosylmethionine (SAM) in a multitude of pathways, *Chlamydia* paradoxically appear to lack the MTAN enzyme needed to salvage products of SAM-utilizing reactions.

Analysis of the *C. trachomatis* transcriptome indicates that several of the BLAST-identified futalosine genes are co-transcribed (32). CT263, a protein of unknown function, is co-transcribed along with the predicted MqnD-homolog (CT262). However, BLAST analysis of CT263 fails to identify a single protein of significant similarity outside of *Chlamydia*. As *Chlamydia* are phylogenetically distinct bacteria, we hypothesized that despite an absence of sequence similarity; CT263 could fulfill the nucleosidase enzymatic role (e.g. step 2 in **Fig. 1**) and complete the futalosine pathway.

Despite annotation as a protein of unknown function, the NCBI Conserved Domain Database (CDD) indicated CT263 might contain a provisional nucleosidase domain (PRK05634). In order to gain further support that CT263 could fulfill a role as a nucleosidase and complete the putative futalosine pathway within *Chlamydia*, *ab initio* modeling of CT263 was performed by the protein structure prediction platform I-TASSER (33-35). The highest ranked computational model of CT263 exhibited a C-score of 0.31, which indicates high confidence in model accuracy (C-score > -1.5; (36)). The top 10 structural analogs in the PDB of this model are all MTAN enzymes with RMSD values below 2.50 Å. As computational predictions for CT263 support a potential role as an MTAN enzyme, enzymatic studies using recombinant protein were initiated in order to further investigate these predictions.

Identification of CT263 Substrates and Hydrolyzed Products

MTAN enzymes have been demonstrated to hydrolyze a variety of substrates, including 5′-methylthioadenosine (MTA), *S*-adenosylhomocysteine (SAH) and 6-amino-6-deoxyfutalosine (AFL) (37-39). Typically, these enzymes catalyze N-glycosidic bond hydrolysis between N9 of adenine and C1 of the thioribose. Catalysis occurs upon protonation at N7 of the substrate, and the S_N1-like transition state is captured by a catalytic water (S_N) with loss of the N-ribosidic bond (N9-C1) and release of adenine (40-43). Efficient processing of these substrates is critical for biochemical pathways involving the products of SAM utilization (44,45). Accumulation of MTA is reported to cause feedback inhibition of polyamine biosynthesis (46,47) and SAM-dependent methylation events, while SAH hydrolysis provides precursors for biosynthesis of quorum sensing compounds. Thus, proper MTAN function is essential to bacteria that require these pathways.

Purified recombinant CT263 was incubated with a variety of potential MTAN substrates, including AFL, SAH, MTA and ATP. HPLC analysis of the reaction mixtures post-CT263 addition revealed that only AFL resulted in substrate conversion (**Fig. 2A)**. Reaction mixtures containing SAH or MTA did not result in substrate conversion (*data not shown*), indicating that CT263 does not function as a canonical MTAN. The product peaks generated by HPLC were confirmed via Fourier transform mass spectrometry (**Fig. 2B-D**) to be that of adenine and dehypoxanthinyl futalosine (DHFL). The observed mass of DHFL indicates that the water-bound intermediate was not observed and is likely unstable under these conditions. Catalysis of AFL to adenine and DHFL indicates that CT263 likely functions within the futalosine pathway (**Fig. 1**). However, the absence of MTA/SAH hydrolytic activity suggests that in contrast to the

bioinformatic predictions, CT263 does not function as a prototypical MTAN.

Kinetic Characterization of Wild-Type C. trachomatis CT263

The ability of CT263 to hydrolyze AFL was further investigated under steady-state conditions (**Fig. 3)**. The results of this assay reveal an apparent K_m of 8.3 ± 0.9 μM. The k_{cat} derived from fitting the curve to the equation for substrate inhibition is 0.91 ± 0.3 min^{-1}. Despite the relatively low catalytic efficiency (k_{cat}/K_m value of 1.8 x 10^3 M^{-1} s^{-1}) CT263 is competent for AFL hydrolysis. In the absence of strong selective pressure (e.g. synthesis of secondary metabolites), enzyme catalytic rates typically do not evolve towards maximal levels. The catalytic efficiency of an average enzyme is ~1 x 10^5 M^{-1} s^{-1}; however, enzymes that function within secondary metabolite pathways are, on average, ~30x slower (48). Thus, the enzymatic rate of CT263 is actually in line with the average rate of previously characterized secondary metabolite enzymes.

The catalytic efficiency of MqnB/MTAN enzymes with broader specificity, including both MTA and AFL, is greater. The MTANs from *Campylobacter jejuni* and *Helicobacter pylori* were reported to give k_{cat}/K_m values of 5.3 x 10^5 and 5.4 x 10^6 M^{-1} s^{-1}, respectively (47, 50). Although the k_{cat} value of CT263 is similar, its K_m value is complicated by substrate inhibition, where larger concentrations of AFL inhibit catalysis, with a dissociation constant of 154 μM (**Fig. 3**). It is important to note that enzymes within bacterial vitamin/cofactor pathways typically exhibit modest catalytic capacity. For example, the synthesis of an electron carrier within *Actinomycetes* has a reported k_{cat}/K_m of 2.0 M^{-1} s^{-1} (49), roughly 900x less efficient than CT263. In order to further understand the enzymatic properties of CT263, recombinant protein was entered into crystallization trials so that the catalytic site could be structurally investigated.

1.58 Å Crystal Structure of CT263 from Chlamydia trachomatis

Orthorhombic crystals ($P2_12_12$) of CT263 were grown and the structure was determined by Au-SAD (all molecular replacement phasing attempts with homology models were unsuccessful) and refined against native X-ray diffraction data to a resolution of 1.58 Å (**Table II**). CT263 is comprised of a single, globular domain (**Fig. 4A**) with dimensions approximately 30 × 30 × 45 Å. The mixed α/β fold of CT263 consists of a central core of 10 twisted β-sheets flanked by two sets of paired α-helices with the following topology: β1-α1-β2-β3-β4-α2-β5-β6-β7-β8-β9-α3-β10-α4-α5. Two polypeptides were found within the asymmetric unit. Numbering of all residues in this work reflects their position in the *C. trachomatis* CT263 sequence.

In contrast to all other CT263 structures presented herein, selenomethionine-labeled CT263 crystallized in a different orthorhombic space group ($P2_122_1$). Structural superposition of both experimentally determined CT263 protomers indicates that they are highly similar to each other, with an RMSD of 0.29 Å across all Cα atoms. Additionally, two polypeptides are also found within the asymmetric unit (**Fig. 4B**).

Consistent with a potential enzymatic function, the CT263 structure contains a large, surface exposed cleft (*black circle* in **Fig. 4C**); predominantly formed by α2, α4 and the loop connecting β8-β9. Additionally, the putative active site cleft of CT263 is characterized by a high degree of electronegative charge density (**Fig. 4C**). This striking feature likely reflects an important contribution to substrate binding. Structural superposition of the computational I-TASSER model and X-ray crystal structure of CT263 (**Fig. 4D**) validates the high confidence of the *ab initio* modeling process with an impressive RMSD of 2.0 Å across all Cα atoms. While the core fold of each structure is highly similar, modeled loop regions in the I-TASSER structure are quite different. These model errors likely account for the unsuccessful use of the I-TASSER model in molecular replacement and could potentially reflect the altered enzymatic profile of CT263.

Oligomeric State of CT263 in Solution

As two polypeptides were found within both CT263 and SeMet-CT263 asymmetric units, the protein interfaces and assemblies (PISA) server (28) was used to assess potential modes of oligomerization. The most thermodynamically favorable assembly was predicted to be a dimer; however, PISA analysis indicated multiple potential interfaces could be adopted within either

crystal system. Intriguingly, only one interface is found within both structures (**Fig. 4B**), suggesting it could be physiologically relevant. This interface buries ~536 Å^2 (6% of the available surface area) with a predicted ΔG of -4.1 kcal/mol and exhibits 2-fold crystallographic symmetry (operator: -x+2,-y,z). Several side chains from each protomer are within hydrogen bonding distance (2.5 – 3.4 Å) and along with numerous hydrophobic contacts, stabilize the interface. These interactions include Arg16-Ser19, Gln180-Leu20, Tyr190-Glu184 and Tyr22-Glu184. Additionally, the side chains of Phe187 from each protomer participate in π-π bonding (**Fig. 4B**). In order to provide support for this dimer, the oligomeric state of CT263 was further analyzed in solution.

Analytical gel filtration chromatography (aGFC) was used to investigate the oligomeric state of CT263 in solution (**Fig. 5A**), which indicated that wild-type CT263 eluted as a single, tailed peak with an apparent molecular mass of 33.7 kDa. This value is much larger than would be expected for monomeric CT263 (~22 kDa), yet smaller than for a dimer (~44 kDa). Reversible association in solution is a common phenomenon with protein oligomeric assemblies. Previous analysis of the effects of reversible dimerization during gel filtration chromatography provides insight into the CT263 chromatogram (50). A tailed peak with a retention time in between those of monomer and dimer, suggests fast dimer association and dissociation, supporting the potential for CT263 to dimerize.

As aGFC analysis of CT263 did not conclusively indicate a dimeric state was adopted in solution, the chemical crosslinker BS^3 (amine-to-amine, 11.4 Å spacer length) was utilized to probe for the formation of higher order complexes (**Fig. 5B**). Incubation of CT263 (50 μM) with 100 μM BS^3 lead to the formation of a single higher order band of the approximate MW for a CT263 dimer. Increasing concentrations of BS^3 failed to produce any higher MW bands (data not shown). All together, these observations provide support that the symmetric CT263 dimer likely exists in solution.

Structural Similarities Suggest CT263 is a 5′-Methylthioadenosine Nucleosidase (MTAN)

The PDB was queried with the protein structure homology server DALI (51) in order to identify functionally characterized proteins that are structurally similar to CT263. The top 5 scoring, unique hits are listed in **Table III**. Each of these structures, as well as the next ~50 hits, is a 5′-methylthioadenosine nucleosidase (MTAN) enzyme. Each of these structures aligns to CT263 with an RMSD of 2.50 Å or lower, and the overall topology of CT263 is consistent with the consensus MTAN fold (**Fig. 6A**). These observations are consistent with the high degree of structural similarity between the CT263 computational model and crystal structures.

There are several notable structural differences between CT263 and the queried MTANs (four regions highlighted in **Fig. 6**) that could potentially account for the altered enzymatic profile of CT263. Helix α2 typically involves at least 4 turns in prototypical MTANs, yet only completes 2 turns within CT263 (region 1 in **Fig. 6A**). Perhaps the most pronounced structural difference within CT263 is found within the loop region connecting β6-β7 (region 2 in **Fig. 6A**). This region is typically involved in dimerization (**Fig. 7**) where it contributes side chains involved in active site interactions within all structurally characterized MTANs (41,52-58). The absence of this region reflects the altered CT263 dimer assemblies relative to the prototypical MTAN dimer interface. Within canonical MTANs the loop connecting β7-β8 is typically α-helical (region 3 in **Fig. 6A**; α3 in *E. coli* MTAN in **Fig. 6B**); however, this region is comprised of random coil in CT263. The role of α3 in prototypical MTAN functionality is currently unclear. Finally, region 4 of CT263 also adopts a random coil conformation instead of α-helical structure. This region is involved in the canonical MTAN dimer interface. Despite these numerous peripheral structural differences, the core fold of CT263 clearly resembles prototypical MTANs.

The high degree of structural conservation between CT263 and prototypical MTANs is remarkable given the absence of significant sequence-level homologs to CT263. Multiple sequence alignment of CT263 with the most structurally similar MTANs (**Fig. 6B**) identified by DALI (highest sequence identity: *A.* thaliana MTAN, 17%; **Table III**) provides a plausible explanation for the absence of the canonical MTAN dimer interface. CT263 is comprised of 196 amino acids, while the shortest MTAN

analyzed in this study (*Staphylococcus aureus*, PDB ID: 3BL6) was comprised of 228 amino acids. Multiple sequence alignment indicates that the majority of this difference is localized to a single contiguous stretch of CT263 (primarily involving regions 2 and 4 in **Fig. 6**). Additionally, the residues that are present within region 3 are in poor sequence-level agreement with the queried MTAN structures.

Even though the prototypical MTAN dimer interface is absent within CT263, the amino acids that are highly conserved cluster within the surface exposed cleft of CT263 (**Fig. 8A**), as determined by the evolutionary conservation server Consurf (29). Furthermore, the extensively studied catalytic triad of carboxylic acid side chains that are critical for enzymatic MTAN function (41) are conserved in CT263 (*red stars* in **Fig. 6B**) and located within the putative active site cleft. Accordingly, the structural similarities between CT263 and canonical MTANs clearly support the observed nucleosidase activity. In addition, the significant structural differences also provide a plausible explanation for the absence of MTA/SAH hydrolytic activity owing to the absence of dimer-mediated active site interface.

Structural Insights into the CT263 Active Site through Substrate and Product Binding

In order to further investigate the function of CT263 and the nature of substrate binding, AFL was incubated with CT263 prior to crystallization. However, upon inspection of the resulting electron density maps, no unaccounted for density was visible within the putative active sites (data not shown). Thus, in light of the apparent inability of CT263 to efficiently hydrolyze MTA (*substrate image in* **Fig. 8B**), we hypothesized that this compound could be utilized to further investigate the function of CT263 with respect to the nature of substrate binding. Wild-type CT263 was incubated with MTA prior to crystallization, and the resulting crystals diffracted X-rays to 1.45 Å (**Table II**). A single region of unaccounted for electron density was visible up to 5.0 σ within only one active site cleft (**Fig. 8C**) of the asymmetric unit dimer. However, it appears that the incubated substrate was actually hydrolyzed by the crystallized enzyme, as the electron density perfectly accommodated an adenine (ADE) molecule (complex termed WT/ADE, **Fig. 9A**). The same protein sample of wild-type CT263 was used in all crystallization trials, suggesting the adenine molecule was not an artifact of co-purification, a common occurrence in MTAN crystal structures (54,58). Given the kinetic characterization of CT263, MTA hydrolysis was rather unexpected; however, it is noteworthy that the time scale of crystallization was significantly longer than the enzymatic assay (18 hour incubation with 250 nM of CT263). This specific catalytic functionality is therefore not likely to be biologically relevant.

Numerous protein contacts are within hydrogen bonding distance of adenine (**Fig. 9A** and **Table IV**), including the side chain of catalytic triad residue Asp161, main chain atoms from Phe72 and Gly74 that are found within a highly conserved region of prototypical MTANs (*blue stars* in **Fig. 6B**), and main chain atoms from Tyr124. The WT/ADE structure is almost identical to the apo-CT263 structure, with an RMSD of 0.50 Å across all residues. However, the loop connecting β8 and β9 has shifted ~1.5 Å towards the substrate, while two side chains (Arg125 and Gln168) near the bound adenine have reoriented (middle panel in **Fig. 9B**), further constricting the active site cleft and reducing solvent exposure to the bound product.

In pursuit of a non-hydrolyzed enzyme-substrate complex, Asp161 was mutated to Asn ($CT263^{D161N}$), a substitution that has previously proven adventitious in obtaining enzyme-substrate complexes (41,57). $CT263^{D161N}$ was expressed, purified and crystallized in essentially the same manner as wild-type CT263. The structure of apo-$CT263^{D161N}$ was determined to 1.27 Å (**Table II**) and shares near-identity with wild-type CT263 giving an RMSD of 0.28 Å across all residues. MTA was incubated with mutant $CT263^{D161N}$ prior to crystallization, and the resulting crystals diffracted X-rays to 1.75 Å (**Table II**). In contrast to wild-type enzyme, the substrate appeared to be intact as a larger region of contiguous electron density was again apparent within only a single active site of the $CT263^{D161N}$ asymmetric unit dimer (**Fig. 8D**). Unexpectedly, the mutant-substrate complex (termed $CT263^{D161N}$/MTA) remained in a nearly identical structural conformation as ADE-bound wild-type CT263, as judged by structural alignment (RMSD values of 0.35 Å across all residues). The same residues

that reoriented in the WT/ADE structure are in identical positions in the CT263^{D161N}/MTA structure. Additionally, interactions with the purine base of MTA are equivalent to those described in the WT/ADE complex. Importantly, the bonding distances between mutant Asn161 and bound ligand (2.6 Å/N7 and 2.9 Å/N6 for WT/ADE and 3.1 Å/N7 and 3.1 Å/N6 for CT263^{D161N}/MTA) are much longer in the mutant complex, indicating proton donation to N7 of the adenine moiety is likely significantly reduced by this substitution.

Protein contacts with the MTA sugar moiety (**Fig. 9C**, **Table IV** and *green star* in **Fig. 6B**) involve hydrogen bonding interactions between the ribosyl 2′- and 3′- hydroxyls and both Glu138 oxygen atoms as well as the main chain nitrogen of Met137 (an invariant MTAN residue). The nucleoside region of MTA adopts a C4′-*endo* sugar pucker and a *syn* ribosidic bond, indicative of a high energy conformation. Identification of the catalytic water is slightly confounded by the presence of four waters at the base of the active site cleft (*red spheres* in **Fig. 9C**). The presence of a 'water-wire' channel for the catalytic nucleophile was previously observed in *Salmonella enterica* MTAN (*Se*MTAN, (54)). Within the CT263^{D161N}/MTA structure, only one of these four waters is within appropriate bonding distance of the catalytic triad residue Glu13 (2.6 Å) and C1 (3.6 Å) of MTA (*large red sphere* in **Fig. 9C**), indicating this water is the most likely S_N candidate.

The 5′-alkylthio side chain of MTA lacks any noticeable hydrogen bonding interactions with CT263^{D161N}, however the side chain of Trp48 forms a hydrophobic barrier parallel to this region of MTA (**Fig. 9C**; distance of ~3.8 Å at each atom). Intriguingly, side chain density for Trp48 was disordered in all previously discussed structures (including SeMet-CT263). This indicates that the presence of MTA increases protein order within CT263. Active site stabilization in CT263 gives some insight into the potentially unique mechanism of CT263-substrate binding, as this aromatic residue is absent from prototypical MTANs (*black star* in **Fig. 6B**). Typically, MTANs encode an aromatic side chain (Phe/Tyr) on a loop from the second monomer, which occludes the active site of the first monomer upon substrate binding (**Fig. 7**). In *Se*MTAN the 5′-alkylthio side chain of the transition state inhibitor MT-DADMe-ImmA was not within hydrogen bonding distance of this aromatic residue (Tyr107), instead extension of the 5′-alkylthio side chain by three carbons placed the ligand within hydrogen bonding distance of this residue (54). Providing further support for a unique role in substrate binding, Trp48 is conserved throughout all chlamydial orthologs of CT263 (*red star* in **Fig. 10**). All together these observations suggest that Trp48 could potentially account for the lack of dimer mediated contacts at the 5′-alkylthio binding site within CT263.

Structural Comparison with SeMTAN Reveals that CT263 is in the Closed Form

MTANs have been extensively studied from a structure/function standpoint in a variety of medically relevant pathogens, including *Escherichia coli* (41,56,58), *Helicobacter pylori* (52,53,57,59), *Staphylococcus aureus* (60) and *Salmonella enterica* (54), among others. All of these structures have crystallized with a conserved dimer interface (**Fig. 7**), involving a region that is absent within CT263 (regions 2 and 4 within **Fig. 6**). The absence of this interface within CT263 resulted in the potential presence of novel dimeric contacts (**Fig. 4B**). The presence of a single occupied active site in substrate bound complexes, as described within the ligand-bound CT263 structures, is quite common in prototypical MTANs (52,54,59). The recent structure of ligand-bound *Se*MTAN highlights this effect, where one monomer was in the 'closed' form while the other remained empty and in the 'open' form (54). Structural superposition of both 'open' and 'closed' *Se*MTAN monomers and the substrate-bound CT263^{D161N}-MTA monomer (**Fig. 11**) indicates that CT263 is in a similar conformation as ligand-bound *Se*MTAN (RMSD of 1.90 Å and 2.05 Å for 'closed' and 'open' conformations, respectively), particularly within the active site cleft (*boxed region* in **Fig. 11**). As the CT263^{WT} and CT263^{D161N}-MTA structures adopted highly similar conformations, these observations suggest that CT263 is constitutively found in a 'closed'-form conformation that is the substrate binding competent.

Molecular Modeling of 6-amino-6-deoxyfutalosine Binding

Despite the fact that MTA was hydrolyzed within wild-type CT263 crystals, enzymatic analysis of CT263 indicates a preference for the futalosine pathway intermediate (**Fig. 1**), 6-amino-6-deoxyfutalosine (AFL). Efforts to co-crystallize $CT263^{D161N}$ with AFL failed to reveal novel regions of electron density in either active site cleft. However, given that the adenosyl moiety is structurally conserved across MTA, SAH and AFL, the $CT263^{D161N}$-MTA complex was used to model the binding location of AFL within the CT263 active site cleft (**Fig. 12**). As the structure of CT263 appears to represent a 'closed'-form conformation, residues contributing to binding of the aromatic isophthalic acid group of AFL are likely close to their current position. The only residue within this region capable of π-π bonding with the benzene ring of AFL is Trp48, the position of which is supported by the CT263-AFL model and D161N-MTA complex. Additional binding specificity could originate from Lys172 and Lys175 (found on either side of the α4-α5 kink), which are appropriately positioned to interact with the carboxylic acid moiety of AFL. Further studies exploring AFL binding could provide insights into the development of specific transition-state inhibitors and anti-chlamydial compounds.

DISCUSSION

In order for a functional electron transport chain to assemble within *Chlamydiaceae*, lipid-soluble electron carriers (e.g. quinones) must be present. The potential source of quinones within *Chlamydiaceae* has yet to be established, with early speculation that they were scavenged from the host (10). However, the presence of a host scavenging translocator or complete quinone biosynthetic pathway was not revealed upon genomic sequencing. Here we provide the first experimental evidence that *Chlamydiaceae* can synthesize MK through the futalosine route, for potential use during oxidative cellular respiration.

While the crystal structure of CT263 displays a high level of structural similarity with MTANs (**Fig. 6A**), the enzymatic characterization of CT263 indicates that only AFL can be hydrolyzed at a physiological rate. Traditionally MTANs hydrolyze intermediates of SAM utilization pathways (37-39), which include substrates that were not processed by CT263 (e.g. MTA and SAH, **Fig. 9B,C**). *Chlamydiaceae* lack the apparent homologs necessary to process the products of MTAN-cleaved MTA and/or SAH (61), however the presence of a conserved SAM/SAH antiporter (31) potentially alleviates the need for CT263 to deal with these metabolites and could account for the apparent lack of this enzymatic function.

We have provided structural evidence that CT263 adopts a novel dimer interface (**Fig. 4B**) compared to prototypical MTANs, and that a single indel (*region 2* within **Fig. 6B)** is responsible for the missing region. Typically, upon substrate binding the MTAN active site is stabilized by both polypeptides of the dimer, with the residues responsible for interaction with the 5′-alkylthio moiety (*dashed box* in **Fig. 7**) coming from the region absent in CT263. Conversely, as the presented ligand-bound CT263 structures reveal, the nucleoside-binding pocket is highly similar to prototypical ligand-bound MTANs (**Fig. 11**). Thus, the presence of a unique Trp (residue 48 within CT263, *black star* in **Fig. 6B**) within the active site pocket might provide a stabilizing hydrophobic 'platform' that could account for the lack of dimeric contacts typically present within the active site. The hypothesis that Trp48 is sufficient to stabilize ligand binding is supported by the $CT263^{D161N}$/MTA structure (**Fig. 9C**). However, the presence of this novel active site side chain does not explain the fact that CT263 was unable to efficiently hydrolyze MTA and SAH (**Fig. 9B,C**). These two prototypical MTAN ligands lack the aromatic isophthalic moiety present within 6A6F. Thus, potential π-π bonding interactions with Trp48 could properly position 6A6F for nucleophilic attack in the wild-type enzyme. Further studies exploring the contribution of Trp48 to enzyme catalysis in CT263 are warranted.

Despite numerous similarities with *Chlamydiaceae*, including an obligate intracellular, biphasic developmental cycle, environmental *Chlamydiales* (e.g. *Protochlamydia, Parachlamydia, Waddlia* and *Simkania*, among others) feature enhanced metabolic capabilities (62). Intriguingly, included among these additional pathways is a complete set of genes for the synthesis of MK through the traditional route (e.g. *menA-G*, **Fig. 1**). BLAST

analysis of genes involved in the first four reactions of the futalosine pathway (including CT263) fails to identify any statistically significant targets within the environmental *Chlamydiales*. This indicates that only the traditional MK biosynthetic pathway is present within environmental *Chlamydiales.* As *Chlamydiaceae* and the environmental *Chlamydiales* are the closest evolutionary relatives to each other, the presence of differing pathways is extremely intriguing yet currently unexplained.

Chlamydia genomes have undergone a large degree of reductive evolution; *Chlamydiaceae* more so than environmental *Chlamydiales* given the 2-3 times smaller genomes found within that order (63). The environmental *Chlamydiales* are significantly more metabolically flexible than *Chlamydiaceae,* encoding additional genes involved in sugar utilization, a complete TCA cycle and an expanded ETC, among other pathways (62). As no organism has been found to simultaneously possess both MK biosynthetic pathways, it seems unlikely that the last common chlamydial ancestor (LCCA) encoded both pathways. It seems likely that the traditional MK pathway (e.g. *menA-G*) was encoded by the LCCA, as Men-gene homologs are found within both pathways. Upon diverging from the LCCA, *Chlamydiaceae* members could have independently acquired the first four genes of the futalosine pathway (and lost the corresponding Men genes), potentially as a result of the differing degree of reliance on host metabolites and ATP for energy production between the two orders.

MTANs are required in a diverse array of biosynthetic pathways (37-39) that have yet to be implicated in *Chlamydia* (e.g. polyamine biosynthesis, quorum sensing, DNA methylation, etc.). However, recently Bonner *et al.* have suggested that the synthesis of menaquinone, and thus enzymatic function of CT263, could be essential for *Chlamydiaceae* to maintain in a "persistent" state inside the host cell (64). Persistence is a reversible state of quiescence that *Chlamydiaceae* utilize as an immune evasion strategy (65). These authors speculated that the tryptophan (Trp) content of key proteins could dictate translational profiles during persistence as a means to respond to host cytosol Trp depletion (e.g. IFN-γ and indoleamine dioxygenase activation). Of particular note to this hypothesis, the chorismate and MK pathways exhibit an extreme down-Trp selection in *Chlamydiaceae*, indicating potential importance to survival in the persistent state.

Our structural and kinetic observations indicate that CT263 (and orthologs in other chlamydial species) likely play an essential role in the menaquinone pathway.. The crystal structure of CT263 revealed an active site with increased solvent exposure that resulted from the absence of the prototypical MTAN dimer interface. Furthermore, CT263 required only minimal structural rearrangements for substrate interaction. The structural information presented within in tandem with our emerging knowledge of MTAN-transition state analogs in prototypical MTANs (53,54,56,66), provides a promising starting point for the rational design of CT263-based anti-chlamydials.

ACKNOWLEDGEMENTS

This research was supported by the National Institute of Health (NIH AI079083 and GM041916). Use of the Advanced Photon Source was supported by the U.S. Department of Energy, Office of Science, Office of Basic Energy Sciences under Contact No. DE-AC02-06CH11357, and use of the IMCA-CAT beamline 17-ID by the companies of the Industrial Macromolecular Crystallography Association through a contract with the Hauptman-Woodward Medical Research Institute. Use of the KU COBRE-PSF Protein Structure Laboratory was supported by grants from the National Center for Research Resources (5P20RR017708-10) and the National Institute of General Medical Sciences (8 P20 GM103420-10) from the National Institutes of Health. We acknowledge the Proteomics facility at Albert Einstein College of Medicine for conducting the mass spectroscopy analysis. We thank Brandon L. Garcia for critical reading and discussion of the manuscript. We thank Liang Tang and Haiyan Zhao for assistance with analytical size exclusion chromatography analysis.

REFERENCES

1. Kurosu, M., and Begari, E. (2010) Vitamin K2 in electron transport system: are enzymes involved in vitamin K2 biosynthesis promising drug targets? *Molecules* **15**, 1531-1553
2. Unden, G., and Bongaerts, J. (1997) Alternative respiratory pathways of Escherichia coli: energetics and transcriptional regulation in response to electron acceptors. *Biochim Biophys Acta* **1320**, 217-234
3. Furie, B., Bouchard, B. A., and Furie, B. C. (1999) Vitamin K-dependent biosynthesis of gamma-carboxyglutamic acid. *Blood* **93**, 1798-1808
4. Bentley, R., and Meganathan, R. (1982) Biosynthesis of vitamin K (menaquinone) in bacteria. *Microbiol Rev* **46**, 241-280
5. Meganathan, R. (2001) Biosynthesis of menaquinone (vitamin K2) and ubiquinone (coenzyme Q): a perspective on enzymatic mechanisms. *Vitam Horm* **61**, 173-218
6. Hiratsuka, T., Furihata, K., Ishikawa, J., Yamashita, H., Itoh, N., Seto, H., and Dairi, T. (2008) An alternative menaquinone biosynthetic pathway operating in microorganisms. *Science* **321**, 1670-1673
7. Brooijmans, R., Smit, B., Santos, F., van Riel, J., de Vos, W. M., and Hugenholtz, J. (2009) Heme and menaquinone induced electron transport in lactic acid bacteria. *Microb Cell Fact* **8**, 28
8. Dairi, T. (2009) An alternative menaquinone biosynthetic pathway operating in microorganisms: an attractive target for drug discovery to pathogenic Helicobacter and Chlamydia strains. *J Antibiot (Tokyo)* **62**, 347-352
9. Juul, N., Jensen, H., Hvid, M., Christiansen, G., and Birkelund, S. (2007) Characterization of in vitro chlamydial cultures in low-oxygen atmospheres. *J Bacteriol* **189**, 6723-6726
10. Stephens, R. S., Kalman, S., Lammel, C., Fan, J., Marathe, R., Aravind, L., Mitchell, W., Olinger, L., Tatusov, R. L., Zhao, Q., Koonin, E. V., and Davis, R. W. (1998) Genome sequence of an obligate intracellular pathogen of humans: Chlamydia trachomatis. *Science* **282**, 754-759
11. Zhi, X. Y., Yao, J. C., Tang, S. K., Huang, Y., and Li, W. J. (2014) The futalosine pathway played an important role in menaquinone biosynthesis during early prokaryote evolution. *Genome Biol Evol*
12. Geisbrecht, B., Bouyain, S., and Pop, M. (2006) An optimized system for expression and purification of secreted bacterial proteins. *Protein Expr Purif* **46**, 23-32
13. Doublié, S. (2007) Production of selenomethionyl proteins in prokaryotic and eukaryotic expression systems. *Methods Mol Biol* **363**, 91-108
14. Kabsch, W. (2010) XDS. *Acta Crystallogr D Biol Crystallogr* **66**, 125-132
15. Evans, P. R. (2011) An introduction to data reduction: space-group determination, scaling and intensity statistics. *Acta Crystallogr D Biol Crystallogr* **67**, 282-292
16. (1994) The CCP4 Suite: Programs for Protein Crystallography. Acta Crystallography
17. Adams, P., Grosse-Kunstleve, R., Hung, L., Ioerger, T., McCoy, A., Moriarty, N., Read, R., Sacchettini, J., Sauter, N., and Terwilliger, T. (2002) PHENIX: building new software for automated crystallographic structure determination. *Acta Crystallogr D Biol Crystallogr* **58**, 1948-1954
18. Adams, P. D., Afonine, P. V., Bunkoczi, G., Chen, V. B., Davis, I. W., Echols, N., Headd, J. J., Hung, L. W., Kapral, G. J., Grosse-Kunstleve, R. W., McCoy, A. J., Moriarty, N. W., Oeffner, R., Read, R. J., Richardson, D. C., Richardson, J. S., Terwilliger, T. C., and Zwart, P. H. (2010) PHENIX: a comprehensive Python-based system for macromolecular structure solution. *Acta Crystallogr D Biol Crystallogr* **66**, 213-221
19. Emsley, P., and Cowtan, K. (2004) Coot: model-building tools for molecular graphics. *Acta Crystallogr D Biol Crystallogr* **60**, 2126-2132
20. Emsley, P., Lohkamp, B., Scott, W. G., and Cowtan, K. (2010) Features and development of Coot. *Acta Crystallogr D Biol Crystallogr* **66**, 486-501
21. Painter, J., and Merritt, E. A. (2006) Optimal description of a protein structure in terms of multiple groups undergoing TLS motion. *Acta Crystallogr D Biol Crystallogr* **62**, 439-450

22. Sturm, M. B., and Schramm, V. L. (2009) Detecting ricin: sensitive luminescent assay for ricin A-chain ribosome depurination kinetics. *Anal Chem* **81**, 2847-2853
23. Thompson, J., Higgins, D., and Gibson, T. (1994) CLUSTAL W: improving the sensitivity of progressive multiple sequence alignment through sequence weighting, position-specific gap penalties and weight matrix choice. *Nucleic Acids Res* **22**, 4673-4680
24. Gouet, P., Courcelle, E., Stuart, D., and Métoz, F. (1999) ESPript: analysis of multiple sequence alignments in PostScript. *Bioinformatics* **15**, 305-308
25. Zemla, A. (2003) LGA: A method for finding 3D similarities in protein structures. *Nucleic Acids Res* **31**, 3370-3374
26. Bernstein, F. C., Koetzle, T. F., Williams, G. J., Meyer, E. F., Brice, M. D., Rodgers, J. R., Kennard, O., Shimanouchi, T., and Tasumi, M. (1977) The Protein Data Bank. A computer-based archival file for macromolecular structures. *Eur J Biochem* **80**, 319-324
27. DeLano, W. L. (2002) The PyMOL Molecular Graphics System. **2009**, http://www.pymol.org
28. Rocchia, W., Sridharan, S., Nicholls, A., Alexov, E., Chiabrera, A., and Honig, B. (2002) Rapid grid-based construction of the molecular surface and the use of induced surface charge to calculate reaction field energies: applications to the molecular systems and geometric objects. *J Comput Chem* **23**, 128-137
29. Glaser, F., Pupko, T., Paz, I., Bell, R. E., Bechor-Shental, D., Martz, E., and Ben-Tal, N. (2003) ConSurf: identification of functional regions in proteins by surface-mapping of phylogenetic information. *Bioinformatics* **19**, 163-164
30. Omsland, A., Sager, J., Nair, V., Sturdevant, D. E., and Hackstadt, T. (2012) Developmental stage-specific metabolic and transcriptional activity of Chlamydia trachomatis in an axenic medium. *Proc Natl Acad Sci U S A* **109**, 19781-19785
31. Binet, R., Fernandez, R. E., Fisher, D. J., and Maurelli, A. T. (2011) Identification and characterization of the Chlamydia trachomatis L2 S-adenosylmethionine transporter. *MBio* **2**, e00051-00011
32. Albrecht, M., Sharma, C. M., Reinhardt, R., Vogel, J., and Rudel, T. (2010) Deep sequencing-based discovery of the Chlamydia trachomatis transcriptome. *Nucleic Acids Res* **38**, 868-877
33. Zhang, Y. (2008) I-TASSER server for protein 3D structure prediction. *BMC bioinformatics* **9**, 40
34. Zhang, Y. (2009) I-TASSER: fully automated protein structure prediction in CASP8. *Proteins* **77 Suppl 9**, 100-113
35. Roy, A., Kucukural, A., and Zhang, Y. (2010) I-TASSER: a unified platform for automated protein structure and function prediction. *Nature protocols* **5**, 725-738
36. Zhang, Y., and Skolnick, J. (2004) Scoring function for automated assessment of protein structure template quality. *Proteins* **57**, 702-710
37. Miller, C. H., and Duerre, J. A. (1968) S-ribosylhomocysteine cleavage enzyme from Escherichia coli. *J Biol Chem* **243**, 92-97
38. Choi-Rhee, E., and Cronan, J. E. (2005) A nucleosidase required for in vivo function of the S-adenosyl-L-methionine radical enzyme, biotin synthase. *Chem Biol* **12**, 589-593
39. Della Ragione, F., Porcelli, M., Cartenì-Farina, M., Zappia, V., and Pegg, A. E. (1985) Escherichia coli S-adenosylhomocysteine/5'-methylthioadenosine nucleosidase. Purification, substrate specificity and mechanism of action. *Biochem J* **232**, 335-341
40. Allart, B., Gatel, M., Guillerm, D., and Guillerm, G. (1998) The catalytic mechanism of adenosylhomocysteine/methylthioadenosine nucleosidase from Escherichia coli--chemical evidence for a transition state with a substantial oxocarbenium character. *Eur J Biochem* **256**, 155-162
41. Lee, J. E., Smith, G. D., Horvatin, C., Huang, D. J., Cornell, K. A., Riscoe, M. K., and Howell, P. L. (2005) Structural snapshots of MTA/AdoHcy nucleosidase along the reaction coordinate provide insights into enzyme and nucleoside flexibility during catalysis. *Journal of molecular biology* **352**, 559-574

42. Lee, J. E., Cornell, K. A., Riscoe, M. K., and Howell, P. L. (2003) Structure of Escherichia coli 5'-methylthioadenosine/ S-adenosylhomocysteine nucleosidase inhibitor complexes provide insight into the conformational changes required for substrate binding and catalysis. *J Biol Chem* **278**, 8761-8770
43. Singh, V., Lee, J. E., Nunez, S., Howell, P. L., and Schramm, V. L. (2005) Transition state structure of 5'-methylthioadenosine/S-adenosylhomocysteine nucleosidase from Escherichia coli and its similarity to transition state analogues. *Biochemistry* **44**, 11647-11659
44. Sufrin, J. R., Meshnick, S. R., Spiess, A. J., Garofalo-Hannan, J., Pan, X. Q., and Bacchi, C. J. (1995) Methionine recycling pathways and antimalarial drug design. *Antimicrob Agents Chemother* **39**, 2511-2515
45. Parveen, N., and Cornell, K. A. (2011) Methylthioadenosine/S-adenosylhomocysteine nucleosidase, a critical enzyme for bacterial metabolism. *Molecular microbiology* **79**, 7-20
46. Raina, A., Tuomi, K., and Pajula, R. L. (1982) Inhibition of the synthesis of polyamines and macromolecules by 5'-methylthioadenosine and 5'-alkylthiotubercidins in BHK21 cells. *The Biochemical journal* **204**, 697-703
47. Pajula, R. L., and Raina, A. (1979) Methylthioadenosine, a potent inhibitor of spermine synthase from bovine brain. *FEBS letters* **99**, 343-345
48. Bar-Even, A., Noor, E., Savir, Y., Liebermeister, W., Davidi, D., Tawfik, D. S., and Milo, R. (2011) The moderately efficient enzyme: evolutionary and physicochemical trends shaping enzyme parameters. *Biochemistry* **50**, 4402-4410
49. Zeyhle, P., Bauer, J. S., Kalinowski, J., Shin-ya, K., Gross, H., and Heide, L. (2014) Genome-based discovery of a novel membrane-bound 1,6-dihydroxyphenazine prenyltransferase from a marine actinomycete. *PloS one* **9**, e99122
50. Yu, C. M., Mun, S., and Wang, N. H. (2006) Theoretical analysis of the effects of reversible dimerization in size exclusion chromatography. *Journal of chromatography. A* **1132**, 99-108
51. Holm, L., and Rosenström, P. (2010) Dali server: conservation mapping in 3D. *Nucleic Acids Res* **38**, W545-549
52. Mishra, V., and Ronning, D. R. (2012) Crystal structures of the Helicobacter pylori MTAN enzyme reveal specific interactions between S-adenosylhomocysteine and the 5'-alkylthio binding subsite. *Biochemistry* **51**, 9763-9772
53. Wang, S., Haapalainen, A. M., Yan, F., Du, Q., Tyler, P. C., Evans, G. B., Rinaldo-Matthis, A., Brown, R. L., Norris, G. E., Almo, S. C., and Schramm, V. L. (2012) A picomolar transition state analogue inhibitor of MTAN as a specific antibiotic for Helicobacter pylori. *Biochemistry* **51**, 6892-6894
54. Haapalainen, A. M., Thomas, K., Tyler, P. C., Evans, G. B., Almo, S. C., and Schramm, V. L. (2013) Salmonella enterica MTAN at 1.36 A resolution: a structure-based design of tailored transition state analogs. *Structure* **21**, 963-974
55. Gutierrez, J. A., Crowder, T., Rinaldo-Matthis, A., Ho, M. C., Almo, S. C., and Schramm, V. L. (2009) Transition state analogs of 5'-methylthioadenosine nucleosidase disrupt quorum sensing. *Nat Chem Biol* **5**, 251-257
56. Lee, J. E., Singh, V., Evans, G. B., Tyler, P. C., Furneaux, R. H., Cornell, K. A., Riscoe, M. K., Schramm, V. L., and Howell, P. L. (2005) Structural rationale for the affinity of pico- and femtomolar transition state analogues of Escherichia coli 5'-methylthioadenosine/S-adenosylhomocysteine nucleosidase. *J Biol Chem* **280**, 18274-18282
57. Kim, R. Q., Offen, W. A., Davies, G. J., and Stubbs, K. A. (2014) Structural enzymology of Helicobacter pylori methylthioadenosine nucleosidase in the futalosine pathway. *Acta Crystallogr D Biol Crystallogr* **70**, 177-185
58. Lee, J. E., Cornell, K. A., Riscoe, M. K., and Howell, P. L. (2001) Structure of E. coli 5'-methylthioadenosine/S-adenosylhomocysteine nucleosidase reveals similarity to the purine nucleoside phosphorylases. *Structure* **9**, 941-953

59. Ronning, D. R., Iacopelli, N. M., and Mishra, V. (2010) Enzyme-ligand interactions that drive active site rearrangements in the Helicobacter pylori 5'-methylthioadenosine/S-adenosylhomocysteine nucleosidase. *Protein Sci* **19**, 2498-2510
60. Siu, K. K., Lee, J. E., Smith, G. D., Horvatin-Mrakovcic, C., and Howell, P. L. (2008) Structure of Staphylococcus aureus 5'-methylthioadenosine/S-adenosylhomocysteine nucleosidase. *Acta Crystallogr Sect F Struct Biol Cryst Commun* **64**, 343-350
61. Stephens, R. S., Kalman, S., Lammel, C., Fan, J., Marathe, R., Aravind, L., Mitchell, W., Olinger, L., Tatusov, R. L., Zhao, Q., Koonin, E. V., and Davis, R. W. (1998) Genome sequence of an obligate intracellular pathogen of humans: Chlamydia trachomatis. *Science* **282**, 754-759
62. Omsland, A., Sixt, B. S., Horn, M., and Hackstadt, T. (2014) Chlamydial metabolism revisited: interspecies metabolic variability and developmental stage-specific physiologic activities. *FEMS microbiology reviews*
63. Collingro, A., Tischler, P., Weinmaier, T., Penz, T., Heinz, E., Brunham, R. C., Read, T. D., Bavoil, P. M., Sachse, K., Kahane, S., Friedman, M. G., Rattei, T., Myers, G. S., and Horn, M. (2011) Unity in variety--the pan-genome of the Chlamydiae. *Mol Biol Evol* **28**, 3253-3270
64. Bonner, C. A., Byrne, G. I., and Jensen, R. A. (2014) Chlamydia exploit the mammalian tryptophan-depletion defense strategy as a counter-defensive cue to trigger a survival state of persistence. *Frontiers in cellular and infection microbiology* **4**, 17
65. Beatty, W. L., Morrison, R. P., and Byrne, G. I. (1994) Persistent chlamydiae: from cell culture to a paradigm for chlamydial pathogenesis. *Microbiological reviews* **58**, 686-699
66. Gutierrez, J. A., Crowder, T., Rinaldo-Matthis, A., Ho, M. C., Almo, S. C., and Schramm, V. L. (2009) Transition state analogs of 5'-methylthioadenosine nucleosidase disrupt quorum sensing. *Nat Chem Biol* **5**, 251-257
67. Zhang, Y. (2009) I-TASSER: fully automated protein structure prediction in CASP8. *Proteins* **77 Suppl 9**, 100-113
68. Zhang, Y. (2008) I-TASSER server for protein 3D structure prediction. *BMC Bioinformatics* **9**, 40
69. Roy, A., Kucukural, A., and Zhang, Y. (2010) I-TASSER: a unified platform for automated protein structure and function prediction. *Nat Protoc* **5**, 725-738
70. Hiratsuka, T., Furihata, K., Ishikawa, J., Yamashita, H., Itoh, N., Seto, H., and Dairi, T. (2008) An alternative menaquinone biosynthetic pathway operating in microorganisms. *Science* **321**, 1670-1673
71. Evans, P. (2006) Scaling and assessment of data quality. *Acta Crystallogr D Biol Crystallogr* **62**, 72-82
72. Diederichs, K., and Karplus, P. A. (1997) Improved R-factors for diffraction data analysis in macromolecular crystallography. *Nat Struct Biol* **4**, 269-275
73. Weiss, M. S. (2001) Global indicators of X-ray data quality. *Journal of Applied Crystallography* **34**, 130-135
74. Karplus, P. A., and Diederichs, K. (2012) Linking crystallographic model and data quality. *Science* **336**, 1030-1033
75. Evans, P. (2012) Biochemistry. Resolving some old problems in protein crystallography. *Science* **336**, 986-987

FIGURE LEGENDS

Figure 1. Multiple Routes Towards Synthesis of Menaquinone in Bacteria. The traditional route of menaquinone biosynthesis has been extensively characterized in *E. coli* and involves 7 Men-family enzymes (*upper*). The futalosine route diverges in the first two steps as indicated by blue and red coloring for routes described in *S. coelicolor*/*T. thermophilus* and *C. jejuni*/*H. pylori*, respectively. Menaquinone

biosynthesis in *Chlamydia trachomatis* (CT) is predicted to function with the genes for each step indicated (*lower*; numbered boxes). The yellow-boxed reaction represents the reaction catalyzed by CT263 studied herein. The gray-boxed genes represent Ubi/Men homologs with predicted prenylation (CT219), methylation (CT428) and decarboxylation activity (CT085 and CT220) that could function in the final steps of menaquinone synthesis.

Figure 2. Identification of CT263 Substrates and Hydrolyzed Products. *A,* HPLC reaction traces showing unreacted AFL (black) and the reaction products after addition of CT263 (blue). Reactions were initiated by the addition of CT263 (250 nM) and allowed to react overnight. *B-D*, Mass spectrometry data for the starred peaks in *panel A*. The isolated peaks indicated by the corresponding asterisk were analyzed on a Varian 12T Fourier transform mass spectrometer in both positive and negative modes. *B,* Spectra were obtained in negative mode. Boxed peak corresponds to the calculated mass of adenine. *C,* Spectra were obtained in negative mode. Boxed peaks correspond to the calculated mass of DHFL minus water and AFL. *D,* Spectra were obtained in positive mode. Boxed peaks correspond to the calculated mass of AFL.

Figure 3. Enzymatic Characterization of CT263. Initial rate (lumens/sec) of catalytic activity with increasing concentrations of CT263 *(left)* and plotted as a function of increasing substrate (●, AFL) concentration *(right)*. Rate kinetics (substrate k_{cat} and K_m and product K_{is}) were calculated by fitting to the Michaelis-Menten equation. Assay conditions (luciferase-based) are detailed in the *Experimental Procedures*.

Figure 4. Crystal Structure (1.58 Å) of CT263 from *Chlamydia trachomatis*. *A,* The crystal structure of CT263 is shown in cartoon ribbon format using common rainbow colors (slowly changing from blue N-terminus to red C-terminus). Secondary structure lacking interpretable electron density is shown as dashed line. *B,* Structural superposition of CT263 dimers from $P2_12_12$ (apo- and ligand-bound) and $P2_122_1$ (SeMet) crystals shown in cartoon ribbon format. Wild-type CT263 dimer (gray) is generated by applying the symmetry operator (-x+2,-y,z), while the SeMet-CT263 dimer (red) is found within the asymmetric unit. Phe187 side chains (cyan, balls-and-sticks) participating in π-π bonding and highlight the two-fold symmetry within this interface. C, Surface representation of electrostatic potential, generated by DelPhi (28), of CT263 (same orientation as *panel A*). Color scheme represents regions of negative (*red*) and positive (*blue*) charge density contoured at ±5 *e*/*kT*. Putative active site cleft is highlighted by black circle. *D,* Structural superposition of I-TASSER (67-69) computational model depicted in cartoon ribbon format (blue, α-helices; yellow, β-sheets; random coil, green) and 1.58 Å crystal structure of CT263 (cartoon ribbon format, colored red). Two structures align with an RMSD of 2.0 Å across all Cα atoms.

Figure 5. Analysis of the CT263 Quaternary Structure in Solution. *A,* Purified CT263 was injected onto an analytical gel filtration column (Superdex 75 10/300 GL, GE Life Sciences) and the elution profile (bottom table) was compared to a series of known standards (top table; BioRad) to derive an estimation of protein molecular weight. The standards are shown as black squares (log MW v. elution volume plot, $R^2 = 0.9997$), while CT263 is represented as a white square. *B,* Purified CT263 (50 μM) was incubated with the amine-reactive crosslinking agent BS^3 (100 μM) at room temperature for 60 min, quenched with 100 mM Tris-HCl (pH 7.5) and analyzed by SDS-PAGE. Apparent MW of CT263 monomer and dimer indicated by black arrows. First lane contains protein ladder.

Figure 6. Structure and Sequence Conservation of CT263 and MTAN Members. *A,* Structural superposition of *E. coli* MTAN (PDB ID: 1Z5P, gray) and CT263 (cyan) structures depicted in cartoon ribbon format and translated apart for clarity. Several regions of structural difference are highlighted in red (*E. coli* MTAN) and numbered on each structure. Secondary structure lacking interpretable electron density within CT263 is shown as dashed line (residues 96-101). *B,* Limited structure-based alignment of

CT263 and MTAN members from the DALI search (51) (**Table III**) was generated using ClustalW (23) and rendered with ESPRIPT (24). The numbers above the sequences correspond to *C. trachomatis* CT263. The secondary structure of CT263 is shown above the alignment while the secondary structure of *E. coli* MTAN (PDB ID: 1Z5P) is shown below. Numbered regions correspond to structural differences highlighted in *panel A*. Residues are colored according to conservation (cyan = identical, and purple = similar) as judged by the BLOSUM62 matrix. Red stars below the sequences correspond to catalytic triad amino acid side chains; blue stars correspond to adenine-bound side chains and green stars correspond to ribosyl-bound side chains in the CT263^{D161N}/MTA structure; while the black star corresponds to the active site CT263 side chain that is disordered in the absence of ligand. Accession numbers are detailed in *Experimental Procedures*.

Figure 7. Dimer-mediated Contacts within Prototypical MTANs. Physiologic dimer of MTA-bound *E. coli* MTAN (PDB ID: 1Z5O) shown in cartoon ribbon format. Each protomer is individually colored (orange and cyan). 5′-methylthioadenosine (MTA) molecule (balls-and-sticks, yellow) modeled in each active site. Catalytic triad and dimer-mediated aromatic residues are shown as balls-and-sticks and colored purple. *Inset*, dashed box indicates magnified active site region.

Figure 8. Structural Insights into CT263 Active Site. *A,* Conservation plot of surface-exposed CT263 amino acid side chains, as generated by CONSURF (29). Color scheme depicts strongly conserved side chains in red. Putative active site cleft is highlighted by black circle and catalytic triad residues are labeled (red stars in **Fig. 6B**). *B,* $F_o - F_c$ map (green mesh at 4.0 σ contour) of the fully refined CT263^{WT}/ADE structure in the absence of modeled ligands (ADE shown for clarity). Catalytic triad side chains are depicted as balls-and-sticks (purple). Backbone is depicted in cartoon ribbon format (orange). *C,* 5′-Methylthioadenosine (MTA). *D,* $F_o - F_c$ map (green mesh at 4.0 σ contour) of the fully refined CT263^{D161N}/MTA structure in the absence of modeled ligands (MTA shown for clarity). Coloring is the same as *panel B*.

Figure 9. Ligand-bound Crystal Structures of CT263. *A,* $2F_o - F_c$ map (blue mesh at 1.0 σ contour) of the refined CT263^{WT}/ADE structure with one adenine molecule (balls-and-sticks, yellow) modeled in the active site. Active site side chains within hydrogen bonding distance (2.5 − 3.5 Å) of adenine are depicted as balls-and-sticks (purple) and CT263 backbone is depicted in cartoon ribbon format (orange). Further information on these distances can be found in **Table IV**. *B,* Surface representation of CT263 structures depicting structural changes that occur upon binding ADE (orange surface) or MTA (green surface). Side chain residues for Arg125 and Gln168 reorient upon ligand binding (solid circle). Ordered electron density for Trp48 (dashed circle) is only seen within MTA-bound structure (green). *C,* $2F_o - F_c$ map (blue mesh at 1.0 σ contour) of the refined CT263^{D161N}/MTA structure with one 5′-methylthioadenosine (MTA) molecule (balls-and-sticks, yellow) modeled in the active site. Active site side chains within hydrogen bonding distance (2.5 − 3.5 Å) of MTA are depicted as balls-and-sticks (cyan) and CT263^{D161N} backbone is depicted in cartoon ribbon format (green). Further information on these distances can be found in **Table IV**. Putative catalytic water is shown as a sphere (red).

Figure 10. Multiple Sequence Alignment of CT263 and *Chlamydiaceae* Orthologs. Limited structure-based alignment of CT263 and *Chlamydiaceae* orthologs was generated using ClustalW (23) and rendered with ESPRIPT (24). The numbers above the sequences correspond to *C. trachomatis* CT263. Residues are colored according to conservation (cyan = identical, and purple = similar) as judged by the BLOSUM62 matrix. Stars below the sequences correspond to catalytic triad amino acid side chains (red) or the *Chlamydiaceae*-specific aromatic active site residue Trp48 (black). Accession numbers are detailed in *Experimental Procedures*.

Figure 11. CT263 Structure Naturally Adopts Closed-like Conformation. Structural comparison of CT263^{D161N}/MTA (cyan) and *Salmonella enterica* MTAN 'open' (red) and 'closed' (purple) forms (PDB

ID: 4F1W), depicted in cartoon ribbon format. Respective bound ligands are shown as balls-and-sticks (MTA, cyan and ADE/TEG, purple). Dashed box highlights that CT263 active site is in a structurally similar conformation as the 'closed' form of *S. enterica* MTAN.

Figure 12. Molecular Model of 6-amino-6-deoxyfutalosine (AFL) Binding to CT263 Active Site. 6-amino-6-deoxyfutalosine (yellow, balls-and-sticks) was manually aligned (within COOT (19,20)) on the MTA molecule present within the $CT263^{D161N}$/MTA cocrystal structure. CT263 is depicted in surface representation (20% transparency and colored grey. Side chains within potential interaction distance of the isophthalic moiety are colored purple and labeled. $2F_o - F_c$ electron density (countered at 1.0 σ) corresponding to bound MTA is presented, highlighting structural conservation between AFL and MTA.

TABLES

Table I

Futalosine Gene	Function	*Chlamydia* Genes		BLAST E-value	Seq. Identity (%)	Query cover (%)
SCO4506[a]	MqnA	CT427[c]	CTL0686[d]	7.00E-12	21	95
SCO4327	MqnB	n/a	n/a	---	---	---
SCO4550	MqnC	CT767	CTL0136	1.00E-84	40	85
		CT426	CTL0685	2.00E-55	33	87
SCO4326	MqnD	CT262	CTL0514	4.00E-43	33	91
SCO4556	???[e]	CT428	CTL0687	4.00E-36	36	92
SCO4491	???	CT219	CTL0471	2.00E-36	36	78
SCO4490	???	CT085	CTL0340	2.00E-72	35	90
SCO4492	???	CT220	CTL0472	3.00E-23	28	94
Cj1285c[b]	MqnA2	CT427	CTL0686	1.00E-06	25	64
Cj0117	MTAN	n/a	n/a	---	---	---

[a]SCO = *Streptomyces coelicolor* A3(2)
[b]Cj = *Campylobacter jejuni*
[c]CT = *Chlamydia trachomatis* D/UW-3
[d]CTL = *Chlamydia trachomatis* L2 434/Bu
[e]??? = Genes predicted to be involved in Futalosine pathway by sequence homology (70)

Table II

	CT263 native	CT263 Au	CT263 SeMet	CT263 Adenine	CT263 D161N native	CT263 D161N MTA
PDB ID	4QAQ		4QFB	4QAR	4QAS	4QAT
Data Collection						
Unit-cell parameters (Å)	*a*=65.96,*b*=104.5, *c*=58.31	*a*=65.24,*b*=103.8, *c*=57.92	*a*=60.85,*b*=74.23, *c*=78.06	*a*=65.64,*b*=104.5, *c*=58.21	*a*=65.44,*b*=104.2, *c*=58.15	*a*=65.88,*b*=104.3, *c*=58.22
Space group	$P2_12_12$	$P2_12_12$	$P2_122_1$	$P2_12_12$	$P2_12_12$	$P2_12_12$
Resolution (Å)[1]	55.77 – 1.58 (1.62 – 1.58)	43.31 – 2.60 (2.71 – 2.60)	47.99 – 1.99 (2.03 – 1.9)	65.64 – 1.45 (1.45 – 1.47)	104.15 – 1.25 (1.27 – 1.25)	104.26 – 1.75 (1.78 – 1.75)
Wavelength (Å)	1.0000	1.03969	0.97911	1.0000	1.0000	1.0000
Temperature (K)	100	100	100	100	100	100
Observed reflections	365,303 (17,639)	78,252 (9,308)	153,450 (10,199)	441,820 (19,724)	714,770 (33,502)	271,538 (15,179)
Unique reflections	56,011 (2,751)	12,572 (1,504)	24,951 (1,672)	71,123 (3,459)	110,407 (5,413)	41,202 (2,223)
$\langle I/\sigma(I)\rangle$[1]	14.8 (2.2)	17.2 (4.8)	14.5 (4.1)	15.7 (2.5)	14.5 (1.9)	13.5 (2.0)
Completeness (%)[1]	100.0 (100.0)	99.5 (99.4)	99.4 (95.3)	99.3 (99.5)	100.0 (99.9)	99.9 (99.9)
Multiplicity[1]	6.5 (6.4)	6.2 (6.2)	6.2 (6.1)	6.2 (5.7)	6.5 (6.2)	6.6 (6.8)
R_{merge} (%)[1, 2]	6.0 (85.7)	6.3 (33.6)	7.5 (38.1)	7.6 (92.9)	5.3 (92.1)	8.0 (94.3)
R_{meas} (%)[1, 4]	7.1 (102.0)	7.4 (40.2)	8.9 (45.8)	8.3 (102.8)	5.7 (100.5)	8.7 (102.0)
R_{pim} (%)[1, 4]	3.8 (54.7)	3.9 (16.4)	4.8 (24.8)	3.4 (43.2)	2.2 (39.8)	3.4 (38.6)
$CC_{1/2}$[5]	99.9 (78.6)	99.7 (91.4)	99.7 (92.9)	98.6 (79.4)	99.9 (74.1)	99.9 (78.5)
Phasing						
Anom. Completeness (%)[1]		96.7 (95.9)	92.8 (89.7)			
Anom. Multiplicity[1]		3.2 (3.1)	2.9 (2.8)			
FOM		33.6	27.9			
Refinement						
Resolution (Å)	40.95 – 1.58		39.04 – 1.99	33.45 – 1.45	33.37 – 1.25	43.62 – 1.75
Reflections (working/test)	55,591 (2,840)		23,618 (1,880)	70,635 (3,573)	110,323 (5,516)	41,136 (2,069)
R_{factor} / R_{free} (%)[3]	16.56 / 19.87		16.65/21.16	18.69 / 21.68	17.76 / 19.54	16.56 / 19.57
No. of atoms (Protein/Ligand/Solvent)	2,980/0/234		3,050/0/136	3,007/10/310	3,021/0/419	3,054/20/241
Model Quality						
R.m.s deviations						
Bond lengths (Å)	0.009		0.012	0.010	0.009	0.010
Bond angles (°)	1.026		1.109	1.059	1.071	1.105
All-atom Clashscore	0.17		1.37	0.83	3.25	1.65
Average *B*-factor (Å^2)						
All Atoms	30.4		27.54	21.9	25.3	34.3
Protein	30.0		27.48	21.1	24.1	33.9
Ligand	n/a		n/a	31.4	n/a	37.5
Solvent	36.4		28.79	29.6	34.6	38.6
Coordinate error, maximum likelihood (Å)	0.15		0.19	0.16	0.14	0.19
Ramachandran Plot						
Most favored (%)	97.9		96.3	97.9	97.3	97.9
Additionally allowed (%)	2.1		3.2	2.1	2.6	2.1
Outliers (%)	0.0		0.5	0.0	0.3	0.0

[1]Values in parenthesis are for the highest resolution shell.

[2]$R_{merge} = \Sigma_{hkl}\Sigma_i |I_i(hkl) - \langle I(hkl)\rangle| / \Sigma_{hkl}\Sigma_i I_i(hkl)$, where $I_i(hkl)$ is the intensity measured for the *i*th reflection and $\langle I(hkl)\rangle$ is the average intensity of all reflections with indices hkl.

[3]$R_{factor} = \Sigma_{hkl} ||F_{obs}(hkl)| - |F_{calc}(hkl)|| / \Sigma_{hkl} |F_{obs}(hkl)|$; R_{free} is calculated in an identical manner using 5% of randomly selected reflections that were not included in the refinement (SeMet-CT263 = 8%).

[4]R_{meas} = redundancy-independent (multiplicity-weighted) R_{merge}(15,71). R_{pim} = precision-indicating (multiplicity-weighted) R_{merge}(72,73).

[5]$CC_{1/2}$ is the correlation coefficient of the mean intensities between two random half-sets of data (74,75).

Table III. CT263 DALI Search Statistics

CT263 Structural Homology					
Top 5 (unique) DALI scores					
Protein name	**PDB code**	**Z-score[a]**	**RMSD**	**Cα range[b]**	**% id[c]**
MTAN, *H. pylori*	4BMZ	22.3	2.2	189/230	16
MTAN, *A. thaliana*	2H8G	21.6	2.4	191/246	17
MTAN, *F. philomiragia*	4JOS	21.5	2.3	188/230	13
MTAN, *S. denitrificans*	4JWT	21.4	2.4	191/245	14
MTAN, *S. aureus*	3BL6	20.9	2.4	186/230	16

[a]Similarity score representing a function that evaluates the overall level of similarity between two structures. *Z*-scores higher than 8.0 indicate that the two structures are most likely homologous (51).
[b]Denotes the number of residues from the query structure that superimpose within an explicit distance cutoff of an equivalent position in the aligned structure.
[c]Denotes the percent sequence identity across the region of structural homology.

Table IV. CT263-Ligand Hydrogen Bonding Info

Enzyme		Ligand		
wild-type		Adenine (ADE)		
Amino Acid	Atom	Distance (Å)	Atom	Group
Tyr124	N	3.2	N1	
Tyr124	O	3.2	N6	
Asp161	OD2	2.9	N6	
Asp161	OD2	3.4	N7	
Asp161	OD1	2.6	N7	
Phe72	O	3.5	N9	
Gly74	N	3.3	N7	
D161N		MTA		
Gly74	N	3.5	N7	Adenine
Tyr124	N	3	N1	Adenine
Tyr124	O	3.2	N6	Adenine
Met137	N	2.8	O2'	2' Ribosyl
Glu138	OE1	3.2	O3'	3' Ribosyl
Glu138	OE2	2.7	O3'	3' Ribosyl
Glu138	OE1	3.4	O2'	2' Ribosyl
Asn161	OD1	3.1	N6	Adenine
Asn161	ND2	3.1	N7	Adenine

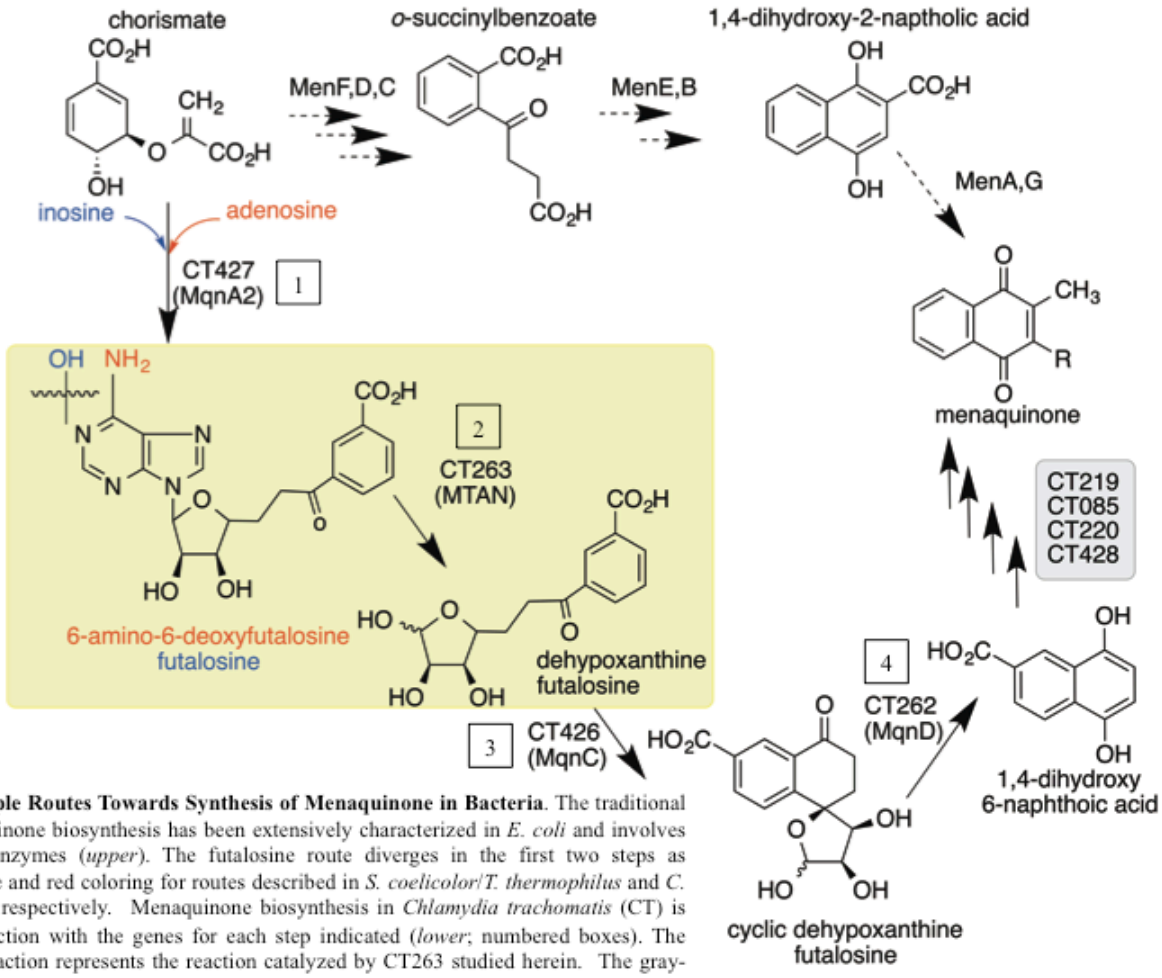

Figure 1. Multiple Routes Towards Synthesis of Menaquinone in Bacteria. The traditional route of menaquinone biosynthesis has been extensively characterized in *E. coli* and involves 7 Men-family enzymes (*upper*). The futalosine route diverges in the first two steps as indicated by blue and red coloring for routes described in *S. coelicolor*/*T. thermophilus* and *C. jejuni*/*H. pylori*, respectively. Menaquinone biosynthesis in *Chlamydia trachomatis* (CT) is predicted to function with the genes for each step indicated (*lower*; numbered boxes). The yellow-boxed reaction represents the reaction catalyzed by CT263 studied herein. The gray-boxed genes represent Ubi/Men homologs with predicted prenylation (CT219), methylation (CT428) and decarboxylation activity (CT085 and CT220) that could function in the final steps of menaquinone synthesis.

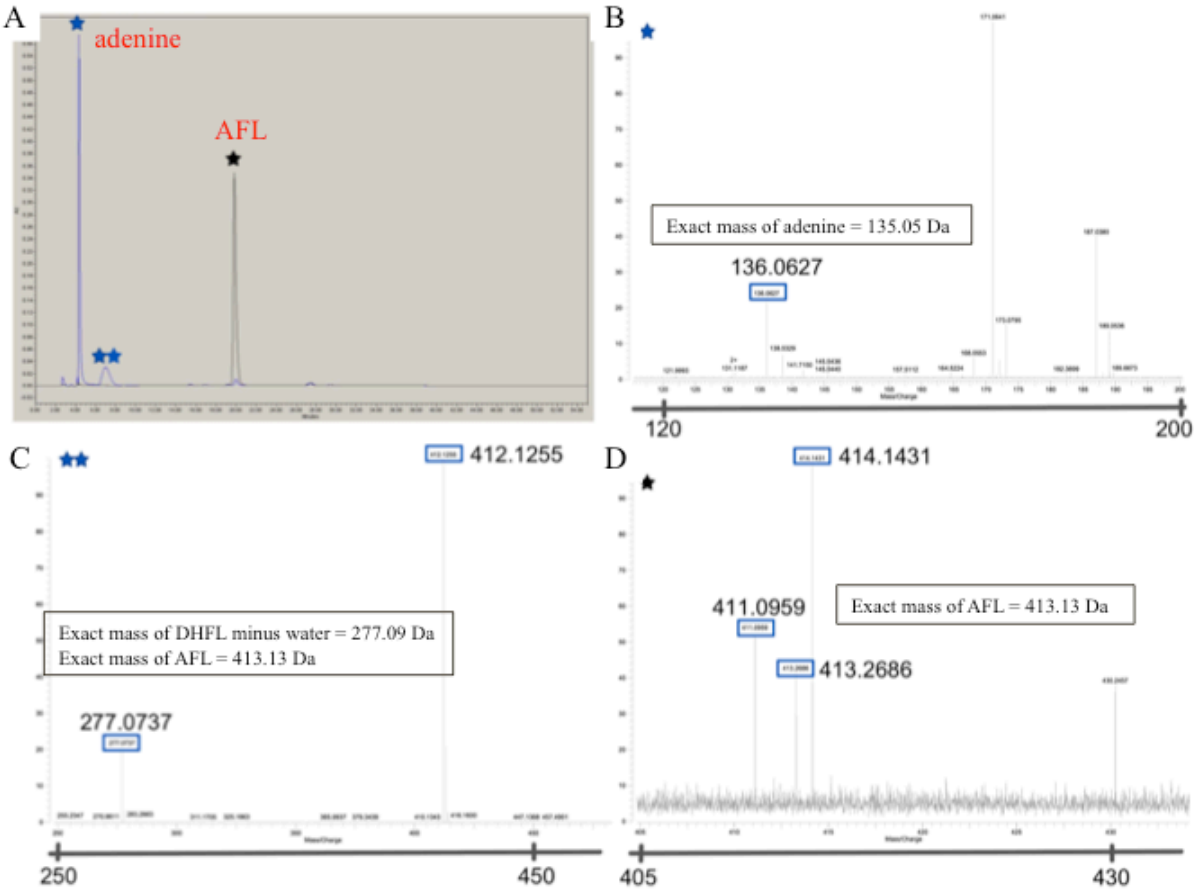

Figure 2. Identification of CT263 Substrates and Hydrolyzed Products. *A,* HPLC reaction traces showing unreacted AFL (black) and the reaction products after addition of CT263 (blue). Reactions were initiated by the addition of CT263 (250 nM) and allowed to react overnight. *B-D,* Mass spectrometry data for the starred peaks in *panel A*. The isolated peaks indicated by the corresponding asterisk were analyzed on a Varian 12T Fourier transform mass spectrometer in both positive and negative modes. *B,* Spectra were obtained in negative mode. Boxed peak corresponds to the calculated mass of adenine. *C,* Spectra were obtained in negative mode. Boxed peaks correspond to the calculated mass of DHFL minus water and AFL. *D,* Spectra were obtained in positive mode. Boxed peaks correspond to the calculated mass of AFL.

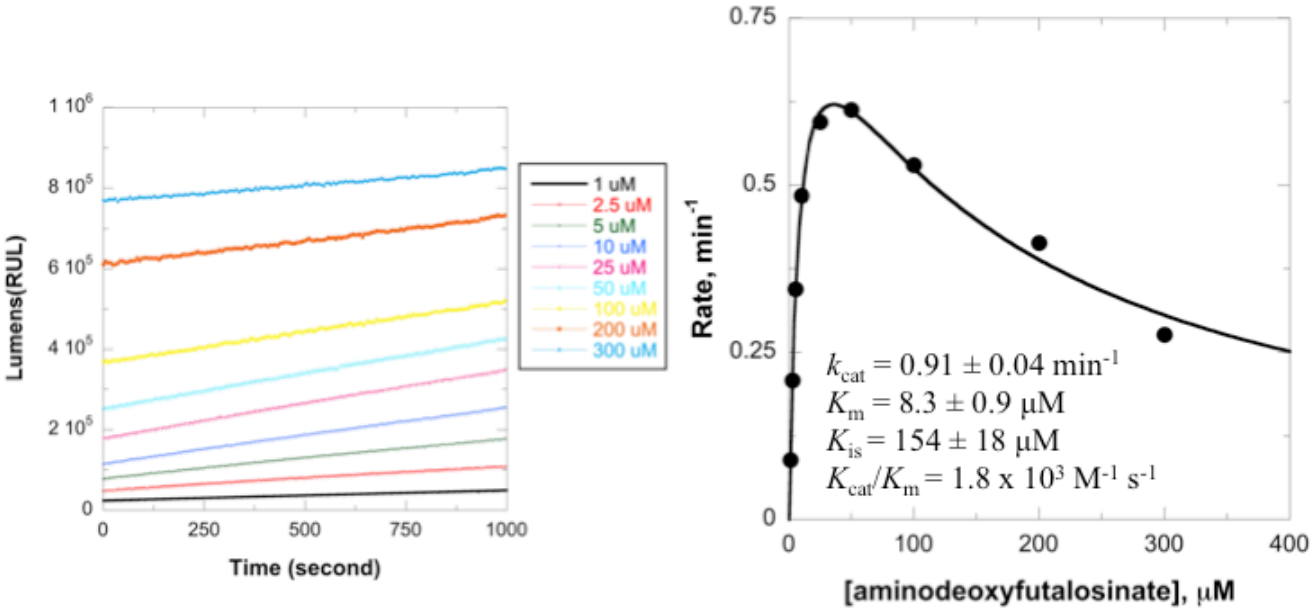

Figure 3. Enzymatic Characterization of CT263. Initial rate (lumens/sec) of catalytic activity with increasing concentrations of CT263 *(left)* and plotted as a function of increasing substrate (●, AFL) concentration *(right)*. Rate kinetics (substrate k_{cat} and K_m and product K_{is}) were calculated by fitting to the Michaelis-Menten equation. Assay conditions (luciferase-based) are detailed in the *Experimental Procedures*.

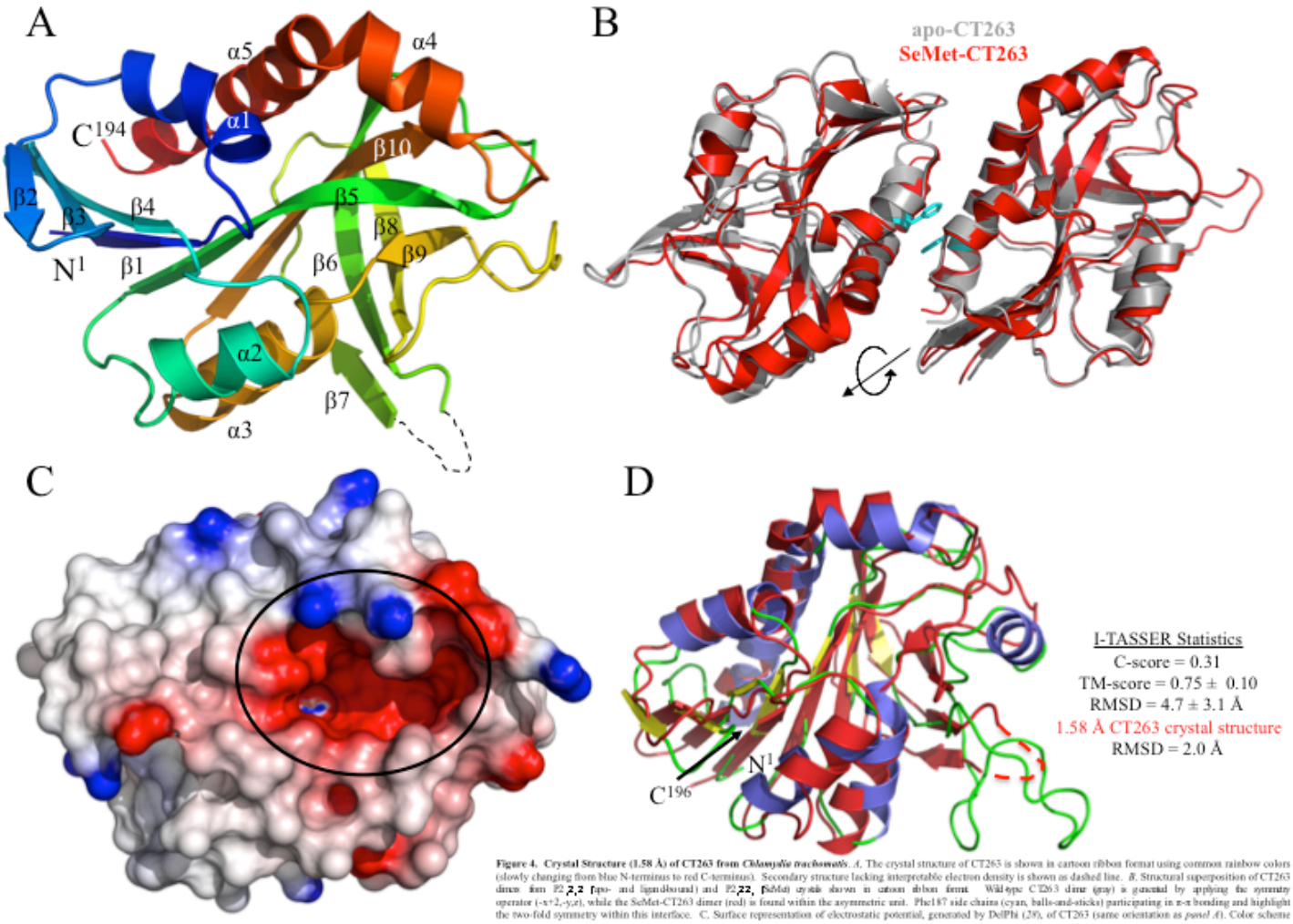

Figure 4. Crystal Structure (1.58 Å) of CT263 from *Chlamydia trachomatis*. *A*. The crystal structure of CT263 is shown in cartoon ribbon format using common rainbow colors (slowly changing from blue N-terminus to red C-terminus). Secondary structure lacking interpretable electron density is shown as dashed line. *B*. Structural superposition of CT263 dimers from $P2_12_12$ (apo- and ligand-bound) and $P2_12_12_1$ (SeMet) crystals shown in cartoon ribbon format. Wild-type CT263 dimer (gray) is generated by applying the symmetry operator (-x+2,-y,z), while the SeMet-CT263 dimer (red) is found within the asymmetric unit. Phe187 side chains (cyan, balls-and-sticks) participating in π-π bonding and highlight the two-fold symmetry within this interface. *C*. Surface representation of electrostatic potential, generated by DelPhi (*29*), of CT263 (same orientation as *panel A*). Color scheme represents regions of negative (*red*) and positive (*blue*) charge density contoured at +5 *e*/*kT*. Putative active site cleft is highlighted by black circle. *D*. Structural superposition of I-TASSER (*64-66*) computational model depicted in cartoon ribbon format (blue, α-helices; yellow, β-sheets; random coil, green) and 1.58 Å crystal structure of CT263 (cartoon ribbon format, colored red). Two structures align with an RMSD of 2.0 Å across all Cα atoms.

A

Sample	Elution Volume (ml)	MW (kDa)	log(MW)
Vitamin B12	18.43	1.35	3.13
Myoglobin	12.75	17.0	4.23
Ovalbumin	10.54	44.0	4.64
IgG	7.89	158.0	5.20

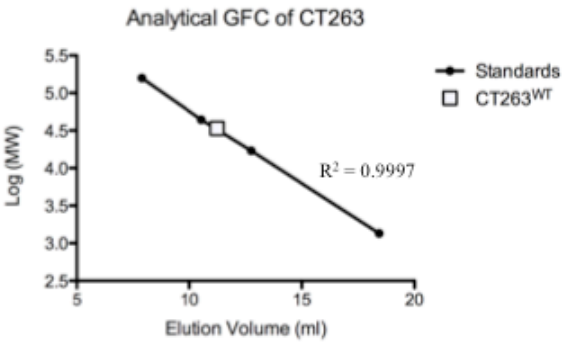

Sample	Elution Volume (ml)	Calculated MW (kDa)	log(MW)
$CT263^{WT}$	11.24	33.7	4.53

B

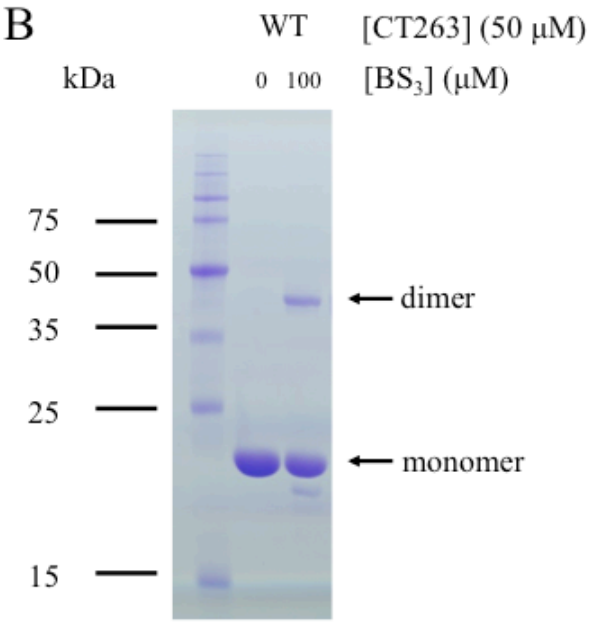

Figure 5. Analysis of the CT263 Quaternary Structure in Solution. *A,* Purified CT263 was injected onto an analytical gel filtration column (Superdex 75 10/300 GL, GE Life Sciences) and the elution profile (bottom table) was compared to a series of known standards (top table; BioRad) to derive an estimation of protein molecular weight. The standards are shown as black squares (log MW v. elution volume plot, R^2 = 0.9997), while CT263 is represented as a white square. *B,* Purified CT263 (50 μM) was incubated with the amine-reactive crosslinking agent BS^3 (100 μM) at room temperature for 60 min, quenched with 100 mM Tris-HCl (pH 7.5) and analyzed by SDS-PAGE. Apparent MW of CT263 monomer and dimer indicated by black arrows. First lane contains protein ladder.

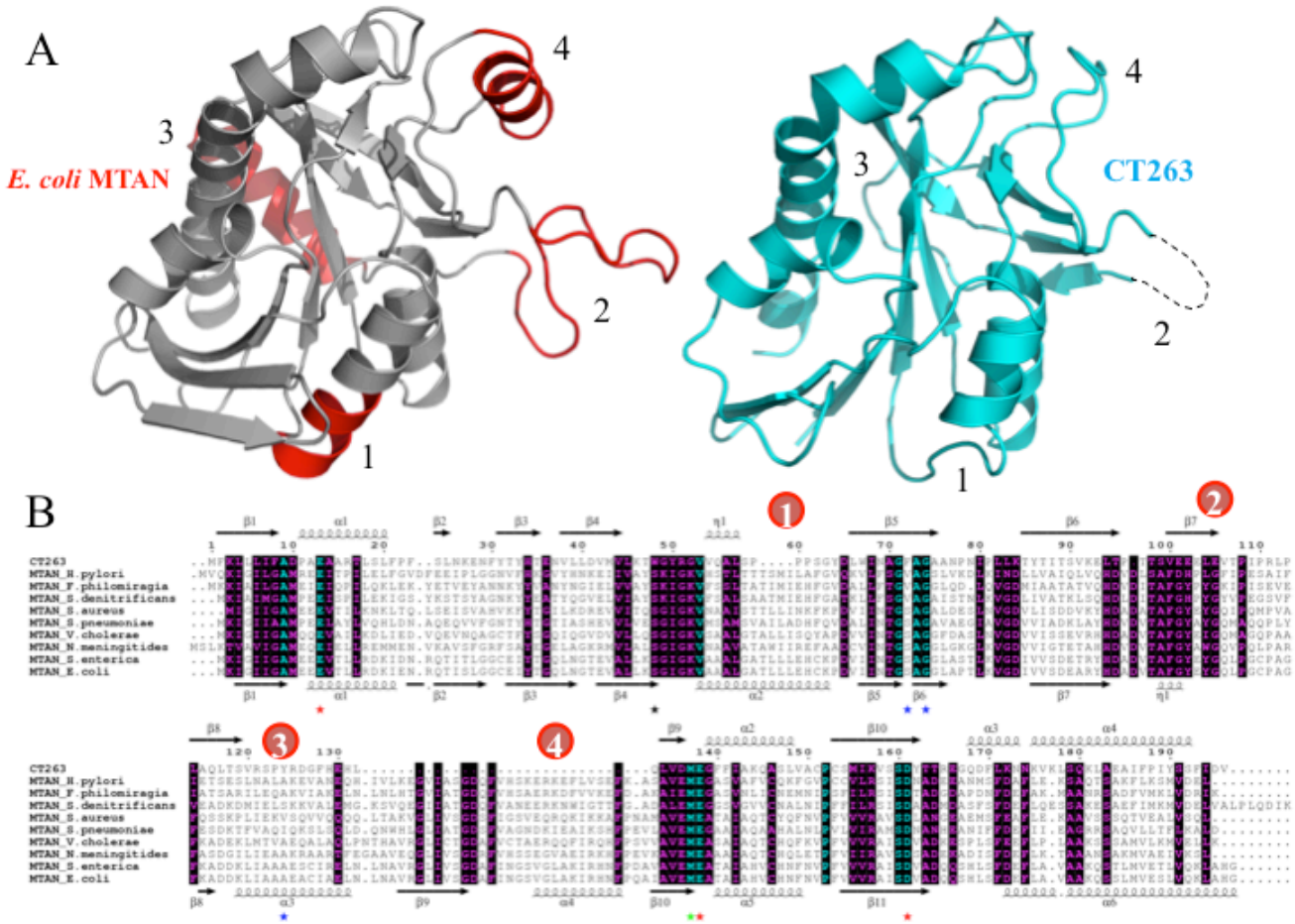

Figure 6. Structure and Sequence Conservation of CT263 and MTAN Members. *A*, Structural superposition of *E. coli* MTAN (PDB ID: 1Z5P, gray) and CT263 (cyan) structures depicted in cartoon ribbon format and translated apart for clarity. Several regions of structural difference are highlighted in red (*E. coli* MTAN) and numbered on each structure. Secondary structure lacking interpretable electron density within CT263 is shown as dashed line. *B*, Limited structure-based alignment of CT263 and MTAN members from the DALI search (*48*) (**Table III**) was generated using ClustalW (*23*) and rendered with ESPRIPT (*24*). The numbers above the sequences correspond to *C. trachomatis* CT263. The secondary structure of CT263 is shown above the alignment while the secondary structure of *E. coli* MTAN (PDB ID: 1Z5P) is shown below. Numbered regions correspond to structural differences highlighted in *panel A*. Residues are colored according to conservation (cyan = identical, and purple = similar) as judged by the BLOSUM62 matrix. Red stars below the sequences correspond to catalytic triad amino acid side chains; blue stars correspond to adenine-bound side chains and green stars correspond to ribosyl-bound side chains in the CT263^{D161N}/MTA structure; while the black star corresponds to the active site CT263 side chain that is disordered in the absence of ligand. Accession numbers are detailed in *Experimental Procedures*.

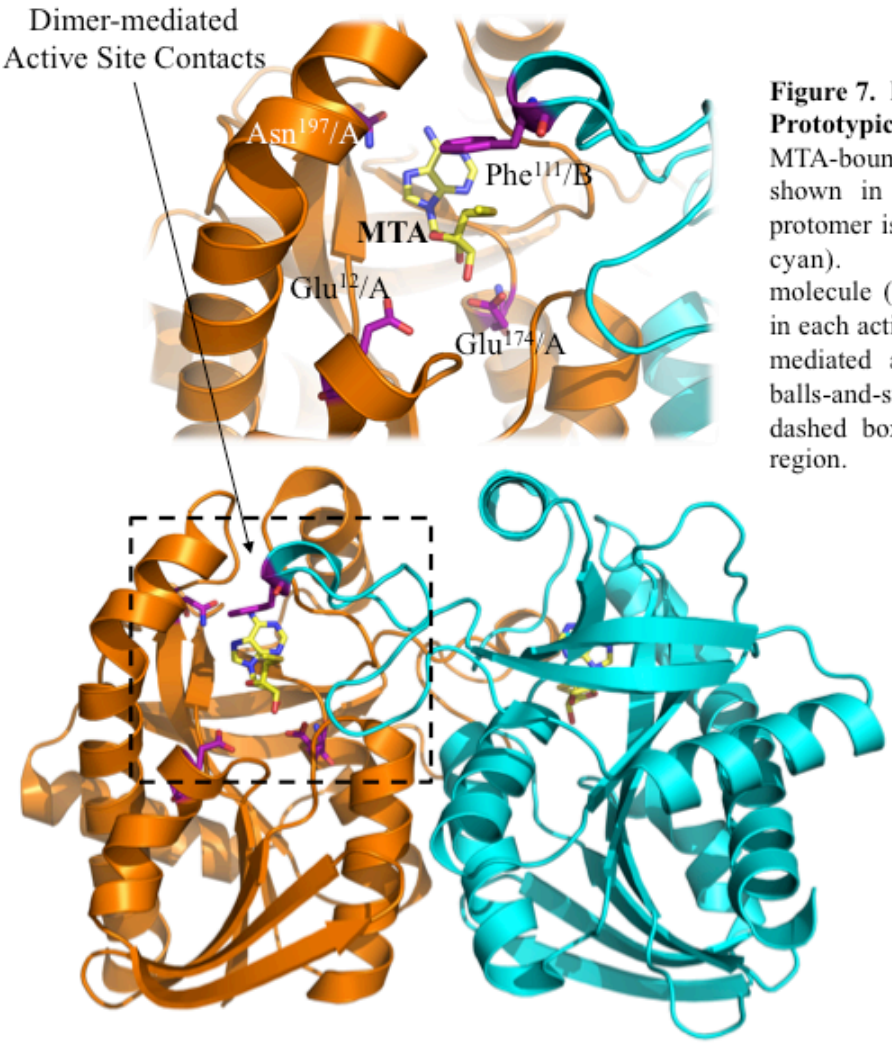

Figure 7. Dimer-mediated Contacts within Prototypical MTANs. Physiologic dimer of MTA-bound *E. coli* MTAN (PDB ID: 1Z5O) shown in cartoon ribbon format. Each protomer is individually colored (orange and cyan). 5′-methylthioadenosine (MTA) molecule (balls-and-sticks, yellow) modeled in each active site. Catalytic triad and dimer-mediated aromatic residues are shown as balls-and-sticks and colored purple. *Inset*, dashed box indicates magnified active site region.

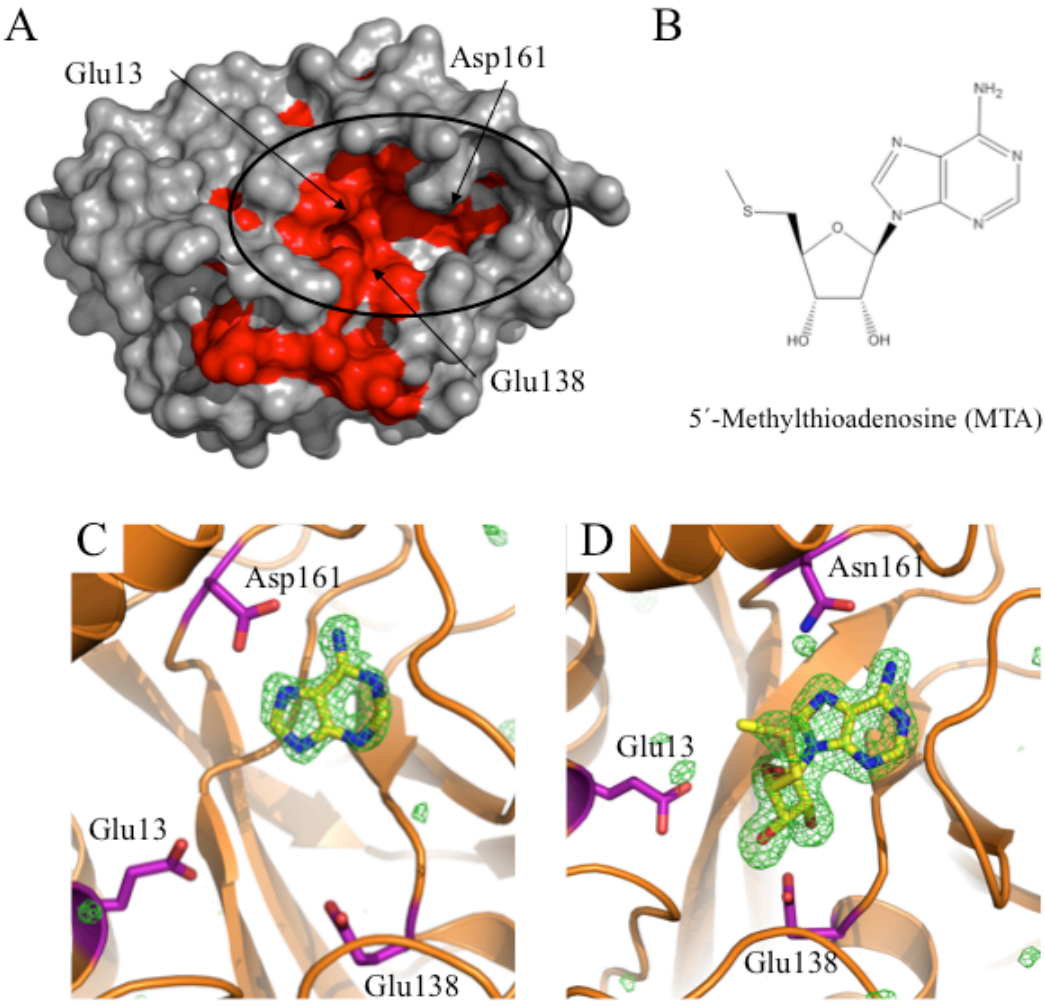

Figure 8. Structural Insights into CT263 Active Site. *A*, Conservation plot of surface-exposed CT263 amino acid side chains, as generated by CONSURF (*29*). Color scheme depicts strongly conserved side chains in red. Putative active site cleft is highlighted by black circle and catalytic triad residues are labeled (red stars in **Fig. 6 B**). *B*, 5′-Methylthioadenosine. *C*, $F_o - F_c$ map (green mesh at 4.0 σ contour) of the fully refined $CT263^{WT}$/ADE structure in the absence of modeled ligands (ADE shown for clarity). Catalytic triad side chains are depicted as balls-and-sticks (purple). Backbone is depicted in cartoon ribbon format (orange). *D*, $F_o - F_c$ map (green mesh at 4.0 σ contour) of the fully refined $CT263^{D161N}$/MTA structure in the absence of modeled ligands (MTA shown for clarity). Coloring is the same as *panel B*.

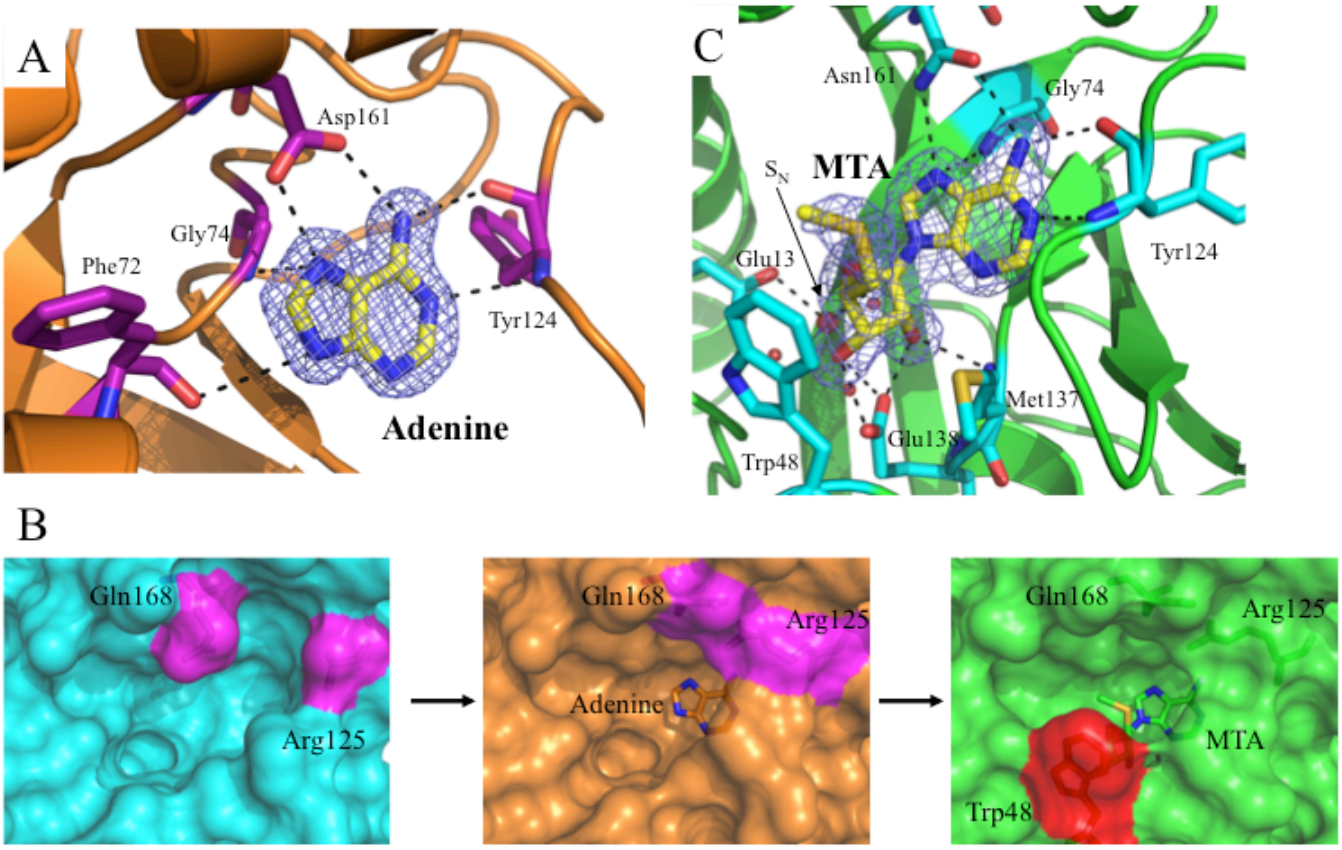

Figure 9. Ligand-bound Crystal Structures of CT263. *A*, $2F_o - F_c$ map (blue mesh at 1.0 σ contour) of the refined $CT263^{WT}$/ADE structure with one adenine molecule (balls-and-sticks, yellow) modeled in the active site. Active site side chains within hydrogen bonding distance (2.5 – 3.5 Å) of adenine are depicted as balls-and-sticks (purple) and CT263 backbone is depicted in cartoon ribbon format (orange). Further information on these distances can be found in **Table IV**. *B*, Surface representation of CT263 (apo-enzyme colored cyan) structures depicting structural changes that occur upon binding ADE (orange surface) or MTA (green surface). Side chain residues for Arg125 and Gln168 (magenta) reorient upon ligand binding (solid circle). Ordered electron density for Trp48 (red) is only seen within MTA-bound structure. Lack of interpretable electron density prevented modeling of Arg125 side chain in the apo-structure. *C*, $2F_o - F_c$ map (blue mesh at 1.0 σ contour) of the refined $CT263^{D161N}$/MTA structure with one 5′-methylthioadenosine (MTA) molecule (balls-and-sticks, yellow) modeled in the active site. Active site side chains within hydrogen bonding distance (2.5 – 3.5 Å) of MTA are depicted as balls-and-sticks (cyan) and $CT263^{D161N}$ backbone is depicted in cartoon ribbon format (green). Further information on these distances can be found in **Table IV**. Putative catalytic water is shown as a sphere (red).

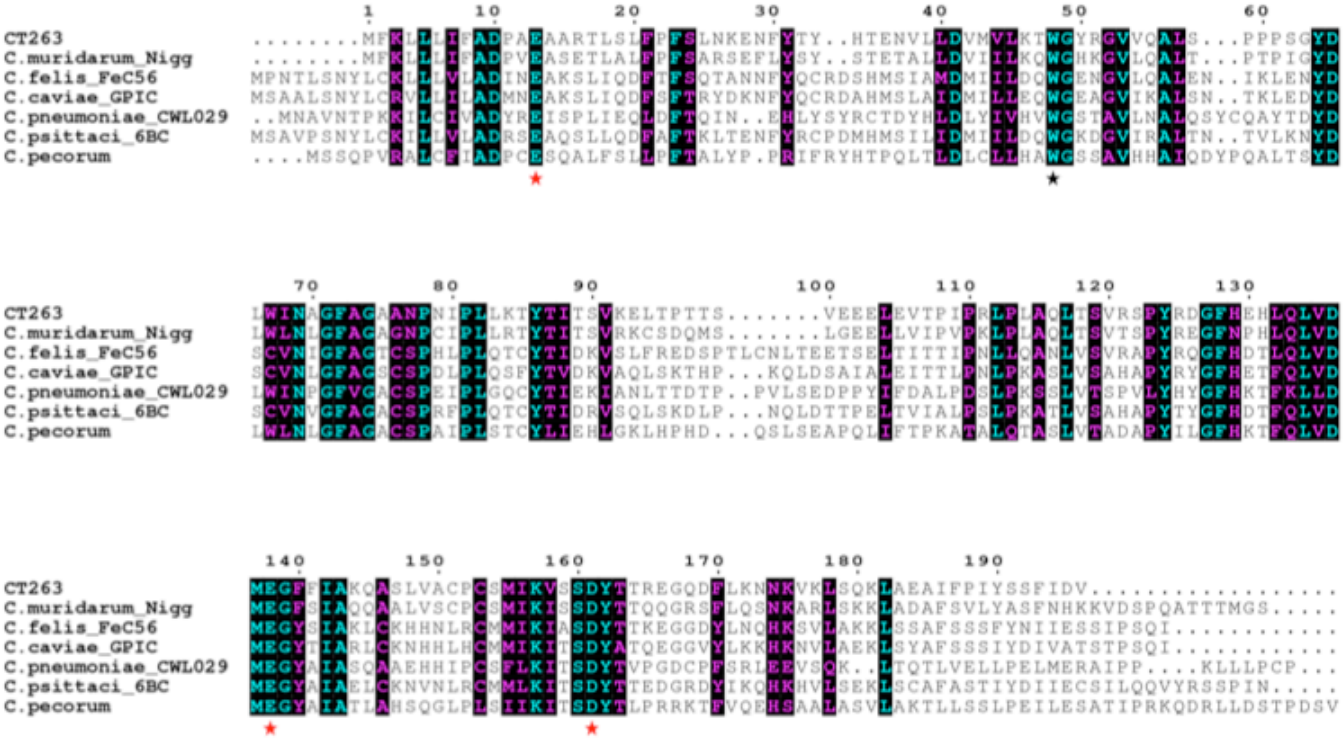

Figure 10. Multiple Sequence Alignment of CT263 and *Chlamydiaceae* Orthologs. Limited structure-based alignment of CT263 and *Chlamydiaceae* orthologs was generated using ClustalW (*23*) and rendered with ESPRIPT (*24*). The numbers above the sequences correspond to *C. trachomatis* CT263. Residues are colored according to conservation (cyan = identical, and purple = similar) as judged by the BLOSUM62 matrix. Stars below the sequences correspond to catalytic triad amino acid side chains (red) or the *Chlamydiaceae*-specific aromatic active site residue Trp48 (black). Accession numbers are detailed in *Experimental Procedures*.

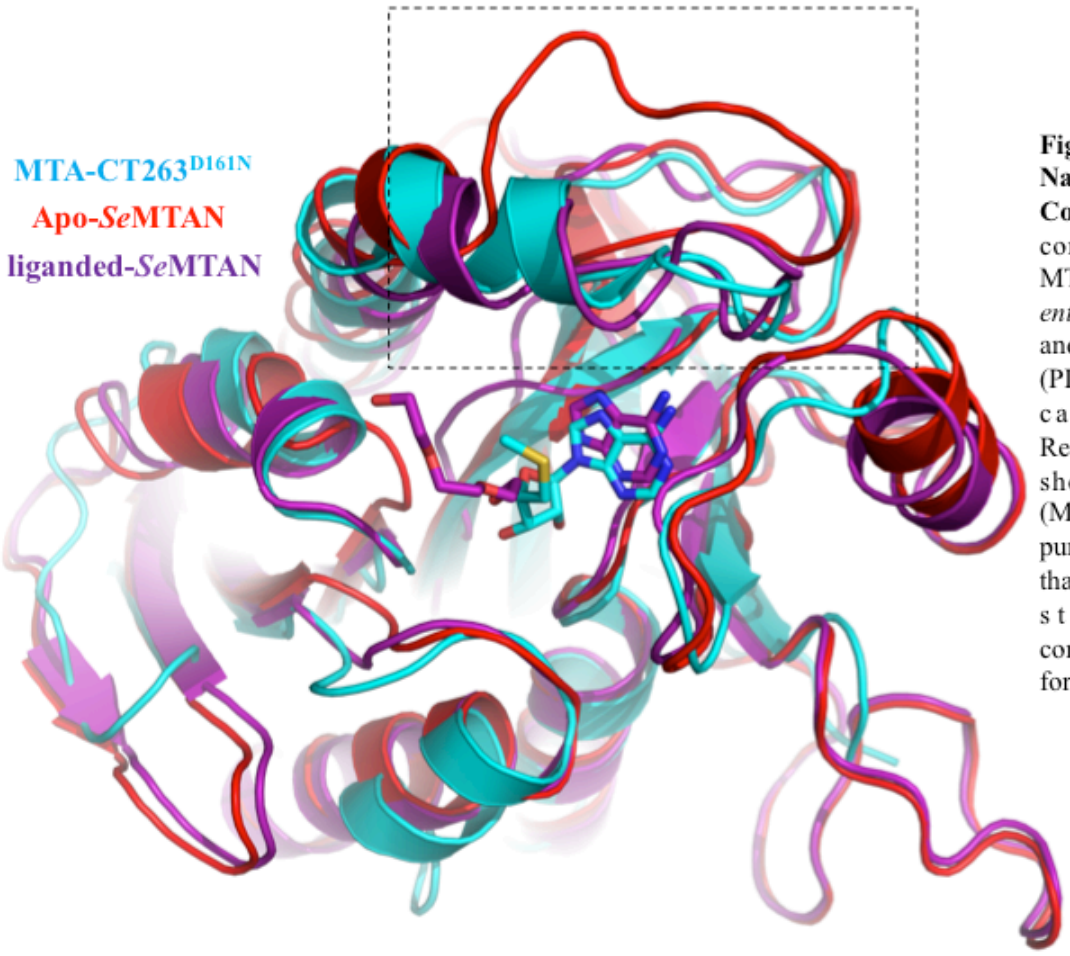

Figure 11. CT263 Structure Naturally Adopts Closed-like Conformation. Structural comparison of CT263^{D161N}/MTA (cyan) and *Salmonella enterica* MTAN 'open' (red) and 'closed' (purple) forms (PDB ID: 4F1W), depicted in cartoon ribbon format. Respective bound ligands are shown as balls-and-sticks (MTA, cyan and ADE/TEG, purple). Dashed box highlights that CT263 active site is in a structurally similar conformation as the 'closed' form of *S. enterica* MTAN.

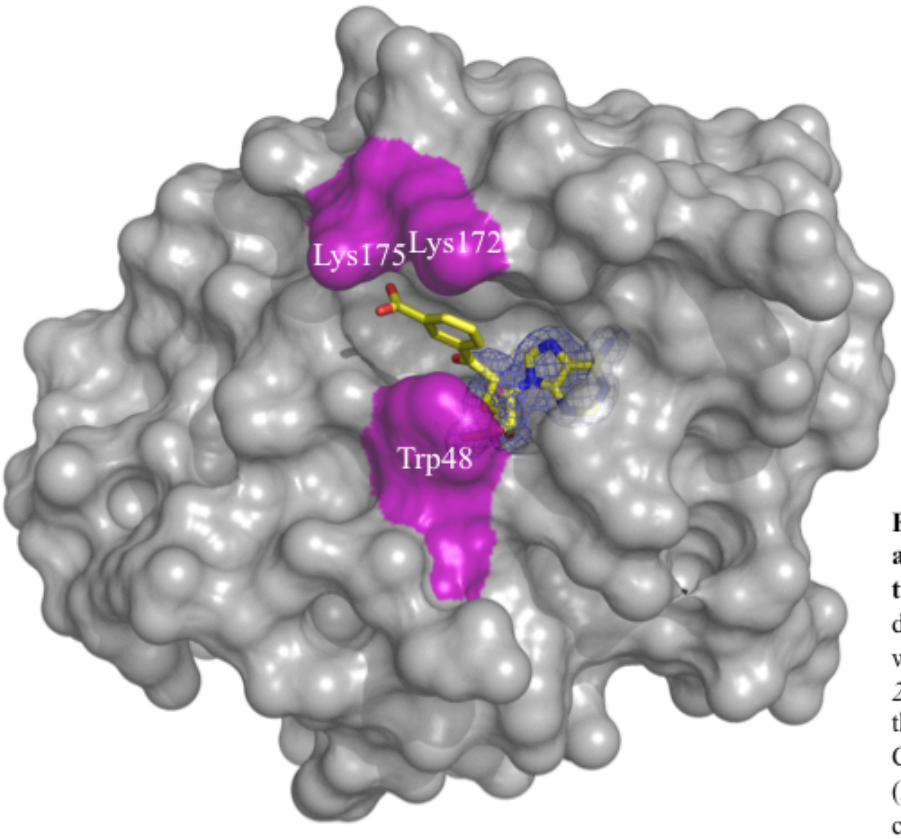

Figure 12. Molecular Model of 6-amino-6-deoxyfutalosine (AFL) Binding to CT263 Active Site. 6-amino-6-deoxyfutalosine (yellow, balls-and-sticks) was manually aligned (within COOT (*19, 20*)) on the MTA molecule present within the $CT263^{D161N}$/MTA cocrystal structure. CT263 is depicted in surface representation (20% transparency and colored grey. Side chains within potential interaction distance of the isophthalic moiety are colored purple and labeled. $2F_o - F_c$ electron density (countered at 1.0 σ) corresponding to bound MTA is presented, highlighting structural conservation between AFL and MTA.